Pre- and *syn*-eruptive conditions of a basaltic Plinian eruption at Masaya Volcano, Nicaragua: The Masaya Triple Layer (2.1 ka)

Emily C. Bamber [a,*], Fabio Arzilli [a], Margherita Polacci [a], Margaret E. Hartley [a], Jonathan Fellowes [a], Danilo Di Genova [b], David Chavarría [c], José Armando Saballos [c], Mike R. Burton [a]

[a] *Department of Earth and Environmental Sciences, The University of Manchester, Oxford Road, Manchester M13 9PL, UK*
[b] *Institute of Non-Metallic Materials, Technische Universität Clausthal, Adolph-Roemer-Straße 2A, 38678 Clausthal-Zellerfeld, Germany*
[c] *Dirección General de Geología y Geofísica, Instituto Nicaragüense de Estudios Territoriales (INETER), Frente a Policlínica Oriental, Managua, Nicaragua*

ABSTRACT

The Masaya Triple Layer tephra was deposited ~2100 years ago during a basaltic Plinian eruption of Masaya caldera, Nicaragua, and is one of few known examples of this extreme endmember of basaltic explosive volcanism. Masaya caldera is located approximately 25 km from Managua, the capital of Nicaragua, and a Plinian eruption presents a high potential risk to its population of 1 million people. Here we use geochemical and petrological tools to constrain the pre- and *syn*-eruptive physico-chemical magmatic conditions, in order to understand how low-viscosity basaltic magmas can erupt with Plinian style.

By combining thermometric models with Rhyolite-MELTS simulations, we find that the Masaya Triple Layer magma was last stored between 1080 and 1100 °C and 21–42 MPa, with a pre-eruptive volatile content of ~2 wt% H_2O. A small phenocryst volume fraction of 0.1 crystallised under water-saturated conditions within a shallow magma reservoir located at 0.8–1.6 km depth. During ascent, rapid microlite crystallisation occurred and lateral velocity gradients across the conduit produced heterogeneous inter-mingling regions of varying crystallinity, between 20 and 50 vol%. Crystal size distribution analysis shows substantial microlite crystallisation over a timescale of 1–5 min, which induced significant changes in viscosity and magma rheology during ascent, increasing the effective magma viscosity from ~10 Pa s to 10^6 Pa s and approaching the brittle fragmentation threshold. Comparable pre- and *syn*-eruptive conditions have been deduced for other examples of basaltic Plinian activity, indicating a common eruption mechanism. We find that the common requirements for a basaltic Plinian eruption are a low magmatic H_2O concentration of ~2 wt%, storage at moderate temperatures of 1080–1100 °C, and rapid crystallisation during magma ascent. Ultimately, these conditions contributed to the production of this highly hazardous Plinian eruption of Masaya.

1. Introduction

1.1. Basaltic Plinian Volcanism

Basaltic volcanism is the most common type of volcanic activity on Earth and throughout the Solar System (Wilson and Head, 1994; Parfitt, 2004). The low viscosity of basaltic magma promotes effusive to mildly explosive Hawaiian and Strombolian eruptions (Parfitt, 2004; Allard et al., 2005; Houghton and Gonnermann, 2008). However, much more explosive basaltic Plinian eruptions can occur when fragmentation takes place relatively deep in the conduit (Moitra et al., 2018). Field studies have classified several sub-Plinian eruptions with ejecta volumes between 0.1 and 1.0 km³ and eruption column heights

of 3–15 km, notably the 2.2 ka eruption of Fuji, Japan; the ~1125–1050 CE eruption of Sunset Crater, Arizona; and the 1999 CE eruption of Shishaldin, Alaska (Newhall and Self, 1982; Stelling et al., 2002; Caplan-Auerbach and McNutt, 2003; Suzuki and Fujii, 2010; Alfano et al., 2018). Examples of basaltic Plinian eruptions where ejecta volumes range between 1.0 and 10.0 km³ and eruption column heights between 10 and 25 km are the 60 ka Fontana Lapilli and 2.1 ka Masaya Triple Layer eruptions of the Las Sierras-Masaya caldera complex, Nicaragua (Williams, 1983; Walker et al., 1993; Pérez and Freundt, 2006; Costantini et al., 2009; Pérez et al., 2009; Zurek et al., 2019); the 122 BCE eruption of Etna, Italy (Coltelli et al., 1998; Houghton et al., 2004); and the 1886 CE Tarawera eruption, New Zealand (Sable et al., 2006; Sable et al., 2009; Kennedy et al., 2010; Schauroth et al., 2016). These eruptions represent the most extreme, yet the least well-understood endmember, of basaltic explosive volcanism. Silicic Plinian eruptions occur approximately once per decade, but the basaltic equivalents have a longer recurrence interval of ~2000 years (Newhall and

Self, 1982; Coltelli et al., 1998; Houghton et al., 2004; Pérez and Freundt, 2006; Costantini et al., 2009). Currently, theoretical conditions for basaltic Plinian volcanism and explosive fragmentation of these low viscosity magmas are poorly understood.

Most Plinian eruptions are silicic and involve fragmentation of ascending magma within volcanic conduits, where the rate of deformation exceeds the rate of structural relaxation of the magma at the glass transition (Dingwell, 1996). Based on the viscoelastic model of Maxwell and estimations of deformation rate during volcanic eruptions, a melt viscosity of 10^6–$10^{6.5}$ Pa s defines the brittle fragmentation threshold (Papale, 1999; Zhang, 1999). Syn-eruptive processes such as extensive crystallisation during magma ascent can significantly increase magma viscosity (Sable et al., 2006; Arzilli et al., 2019). At crystallinities exceeding 50 vol%, magma viscosity is primarily governed by the crystal phase as opposed to the interstitial melt, increasing viscosity and the potential for brittle magma fragmentation (Lavallée et al., 2007).

In contrast, at viscosities $<10^6$ Pa s, analogue decompression experiments find that expansion of entrained gas within bubbly fluids can induce fragmentation of the fluid. This process is termed inertia-driven fragmentation (Namiki and Manga, 2008). For bubbly magmas with high initial water content and inefficient degassing, brittle failure occurs when the tensile stress within bubble walls exceeds the tensile strength of the magma (Zhang, 1999). High initial volatile concentrations have been associated with explosive eruptions (Sable et al., 2006). At Stromboli, the generation and collapse of CO_2-rich foam layers at depth can produce CO_2-rich gas slugs and explosive paroxysmal activity (Allard, 2010; Aiuppa et al., 2011). Assimilation of carbonate wall rock and consequent CO_2 fluxing can modify magma composition and volatile solubility during magma ascent, facilitating volatile exsolution, bubble expansion and an explosive eruption (Dallai et al., 2011; Freda et al., 2011; Cross et al., 2014). The interaction between the CO_2-rich fluxing gas phase and stored CO_2-poor degassed magma within the magma chamber can induce extensive crystallisation through isobaric dehydration. The resulting rheological change can pressurise the system and generate an explosive eruption (Blundy et al., 2010). Finally, external H_2O can also enhance explosivity, such as the explosive 1500 CE Keanakāko'i Tephra phreatomagmatic eruption of Kilauea, Hawaii (Swanson et al., 2012).

The low viscosity (10–10^4 Pa s) and fast relaxation time (10^{-9}–10^{-6} s) of basaltic magmas should enable sufficient structural relaxation of the melt, precluding fragmentation (Parfitt, 2004; Goepfert and Gardner, 2010; Moitra et al., 2018). Previous studies have assessed the influence of *syn*-eruptive crystallisation and degassing efficiency during magma ascent on explosivity for the Fontana Lapilli, Etna 122 BCE and Tarawera eruptions (Giordano and Dingwell, 2003; Del Carlo and Pompilio, 2004; Houghton et al., 2004; Sable et al., 2006; Sable et al., 2009, Costantini et al., 2010; Baker et al., 2012; Szramek, 2016; Moitra et al., 2018). Nevertheless, the fragmentation mechanisms are still strongly debated (Costantini et al., 2010; Goepfert and Gardner, 2010; Szramek et al., 2016). Constraining the pre- and syn-eruptive conditions of these basaltic magmas is therefore critical if we are to understand the driving mechanisms of basaltic Plinian eruptions.

Historical observations of the Etna 122 BCE and Tarawera eruptions suggest that basaltic Plinian activity presents a tangible hazard to the ever-increasing populations living in proximity to these volcanoes (Coltelli et al., 1998; Houghton et al., 2004; Costantini et al., 2009). However, the complex, episodic Masaya Triple Layer eruption remains comparatively understudied, and detailed petrological data on the pre- and syn-eruptive conditions of this Plinian eruption are currently lacking. Here we present new data on the chemical and textural evolution of the Masaya Triple Layer eruption and use geochemical and petrological tools to constrain the conditions and timescales of magmatic storage and syn-eruptive processes for this eruption. Constraining the physico-chemical conditions, including magma storage pressure and temperature, stored volatile concentration, and crystallisation kinetics is critical for understanding the triggering mechanism. This study provides an understanding of the conditions which favoured Plinian activity at Masaya, but also contributes to our general understanding of basaltic Plinian volcanism.

1.2. The Masaya Triple Layer eruption

Masaya caldera is located approximately 25 km from Managua, the capital of Nicaragua. It is one of 18 major volcanic centres of the Nicaraguan Depression, a graben formed from the subduction of the Cocos Plate beneath the Caribbean Plate along the western margin of Nicaragua (Fig. 1a). Masaya is a continuously degassing basaltic caldera (Stoiber et al., 1986; Burton et al., 2000; Duffell et al., 2003), and has produced 26 VEI 1–2 eruptions since 1524. It is one of the most active volcanic complexes in Nicaragua, with an average repose period of 10 years between minor explosive eruptions (Freundt et al., 2006). However, the Las Sierras-Masaya caldera complex has also produced several examples of basaltic Plinian eruptions: notably the Fontana Lapilli and the Masaya Triple Layer (VEI 4–6) (Williams, 1983; Bice, 1985; Pérez and Freundt, 2006; Wehrmann et al., 2006; Costantini et al., 2009; Pérez et al., 2009; Costantini et al., 2010). Masaya has potentially erupted geochemically homogeneous magmas over 30,000 years. Tephra and lava exhibit little compositional variation across explosive-effusive transition of Masaya, from highly explosive basaltic Plinian eruptions, to its current relatively quiescent activity (Walker et al., 1993; Zurek et al., 2019). This homogeneity suggests that no significant change in magma composition is required to induce a drastic change in eruptive style, an important consideration for detecting precursors to Plinian activity.

The Masaya Triple Layer deposit consists of two facies, identical in bulk composition but with distinctive areal distributions and stratigraphic architecture: the La Concepción facies to the south of the caldera, and the Managua facies towards the northwest (Pérez et al., 2009). The proximal La Concepción facies is divided into eight layers of well-sorted basaltic lapilli and ash with intercalated tuffs (Pérez and Freundt, 2006). The eruption model of Pérez et al. (2009) defines 10 discrete phases of a complex, pulsatory eruption. Two Plinian episodes with sustained eruption columns (episodes II and IV of Pérez et al., 2009) are separated by phreatomagmatic activity, minor ash falls, and surges, producing the intercalated scoriae and tuff deposits observed in the field (Kutterolf et al., 2007; Pérez et al., 2009). The estimated total eruptive volume is 3.4 km^3 (DRE 1.8 km^3), using isopach maps constrained by outcrops and offshore deposits (Kutterolf et al., 2007; Kutterolf et al., 2008; Pérez et al., 2009). Estimated column heights of 22–24 km for phase II and 21–23 km for phase IV correspond to mass discharge rates of 10^6–10^8 kg/s for the Plinian stages of the eruption (Pérez et al., 2009).

Considering that three major pyroclastic deposits within the past 6000 years have been attributed to Masaya Volcano, a resurgence of Plinian activity is not implausible (Pérez and Freundt, 2006; Kutterolf et al., 2007; Pérez et al., 2009). Footprints upon a coarse ash surface of the Masaya Triple Layer deposit have been interpreted as tracks of the Acahualinca people escaping the eruption, a community who inhabited the outskirts of present-day Managua (Schmincke et al., 2009; Schmincke et al., 2010). Isopachs of the Masaya Triple Layer eruption currently encompass several major cities in the Managua and Masaya departments (Fig. 1a). According to the 2012 INIDE (Instituto Nacional de Información de Desarrollo) population estimate, 1.8 million people live in this area. The present-day population at risk from highly explosive activity is probably even greater, given population growth and increased urbanisation since 2012. Considering that Masaya caldera exhibits recurrent basaltic Plinian activity, the possibility of a future Plinian eruption cannot be discounted.
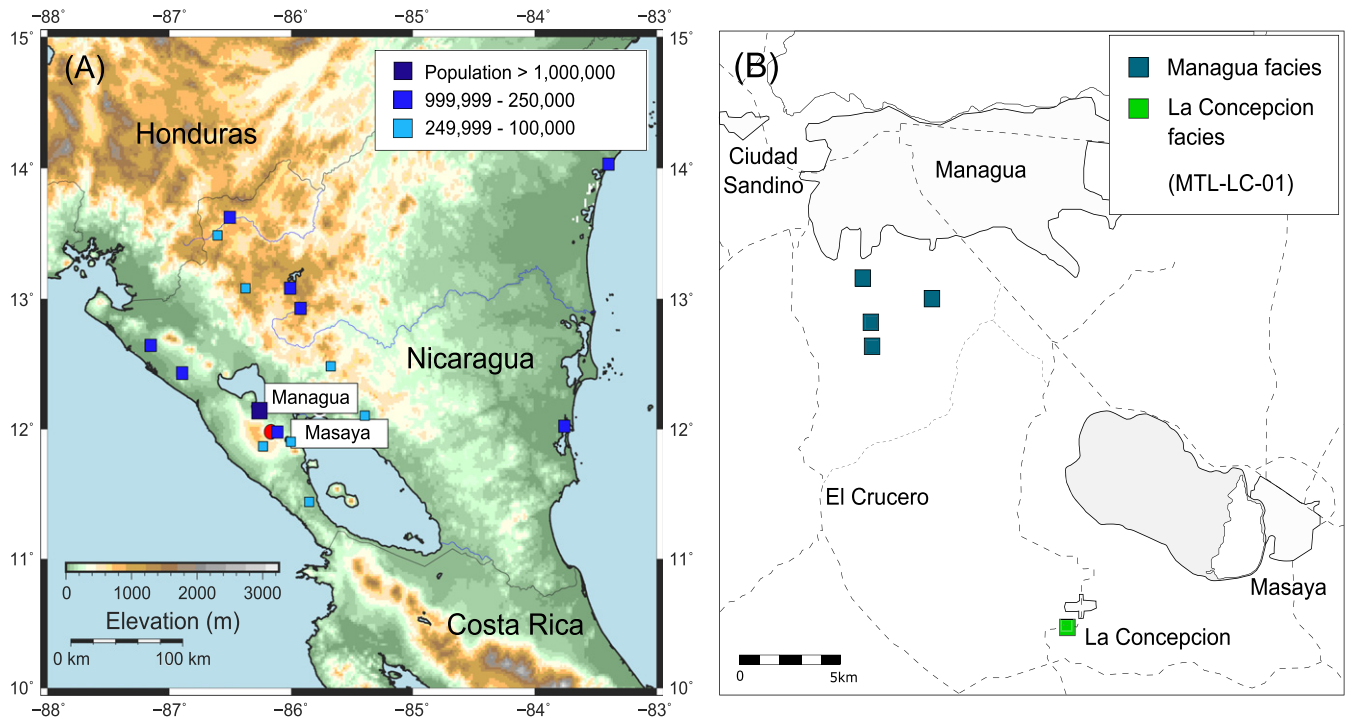
Fig. 1. (a) A map of Nicaragua, showing the location of Masaya caldera as a red circle (Amante and Eakins, 2009). Blue squares show cities with populations >100,000 that could be affected by a Plinian eruption of Masaya. (b) A map of the field area studied, showing the proximity of Masaya caldera to the capital Managua. Sampling sites of the Managua and La Concepción facies are indicated. The green square shows the proximal locality MTL-LC-01.

2. Methods

2.1. Fieldwork

Both the Managua and La Concepción facies were sampled during fieldwork, using the stratigraphic framework of Pérez et al. (2009). An outcrop of the La Concepción tephra deposit, MTL-LC-01 (11°55′ 33.6″N, 86°11′33.4″W), was selected for detailed sample analysis. This site is located approximately 6 km from Masaya caldera, representing a proximal deposit dispersed by tropospheric winds (Fig. 1b) (Pérez and Freundt, 2006; Pérez et al., 2009). As the Managua facies sites sampled are distal with a higher proportion of intercalated tuffs, we focused our analysis solely on the La Concepción facies for the best representation of conduit processes. The facies are identical in bulk composition, but differ in their internal architecture (Pérez et al., 2009); we can therefore reasonably assume that our results from the proximal La Concepción deposit are representative of the Masaya Triple Layer eruption. We divided the deposit into three layers, TLL1, TLL2 and TLL3, to construct a simpler stratigraphic division. This division focuses upon the opening and two main Plinian phases of activity whilst removing intercalated tuff sub-units of phreatomagmatic origin from the analysis, due to their uncertain relation to the eruption dynamics. TLL1 is the opening phase of the eruption (subunit I of Pérez et al., 2009), deposited by a series of magmatic and phreatomagmatic explosions of lower intensity. TLL2 and TLL3 are the major Plinian phases of the eruption (subunits II and IV of Pérez et al., 2009) and were deposited by a sustained eruption column. The opening and the two Plinian stages of the eruption were selected to investigate the temporal evolution of the eruption, and any chemical and microtextural variations that correlate with changes in explosivity (Pérez and Freundt, 2006; Pérez et al., 2009).

We selected 16 scoria clasts for detailed analysis: six from TLL1-A_0 and five each from TLL2-A_0 and TLL3-A_0 (Fig. 2). Two 15 g pressed powder pellets of TLL2 and TLL3 were produced for XRF analysis. We selected a number of clasts from each layer to ensure that we accounted for the textural heterogeneity within the deposit. The bulk geochemical homogeneity of the two facies of the Masaya Triple Layer means that we can be confident that our sample set is representative of the eruption, allowing us to investigate the pre-eruptive magmatic conditions and eruption dynamics. However, this sample set is geographically restricted to a single location of the La Concepción facies, and that textural heterogeneity within and between proximal and distal deposits may introduce some limitations when generalising the conclusions drawn from our dataset.

2.2. Scanning electron microscopy and crystal size distribution analysis

Back-scattered electron (BSE) images were collected using a FEI Quanta 650 FEG-SEM at the Department of Earth and Environmental Sciences, University of Manchester, using an acceleration voltage of 15 kV and a beam current of 10 nA. Sixteen scoriae 1–1.7 cm in size were analysed, to account for potential textural heterogeneities that could have been introduced by variations in cooling rate with clast diameter (Szramek et al., 2010).

We used ImageJ software (Abramoff et al., 2004; Schneider et al., 2012) for textural analysis of BSE images from layers TLL1, TLL2 and TLL3. The area of each crystal phase, glass and bubbles was measured in 2D. Crystal fractions for each mineral phase (ϕ) were then calculated using the vesicle-free area of the sample (A) and the area of each crystal phase (A_x) (Hammer et al., 1999):

$$\phi = \frac{A_x}{A} \tag{1}$$

Crystal number densities (N_a) were calculated for plagioclase and oxides only (where n_{cry} refers to the number of crystals), due to the difficulty of segmenting anhedral mafic phases with comparable image contrast:
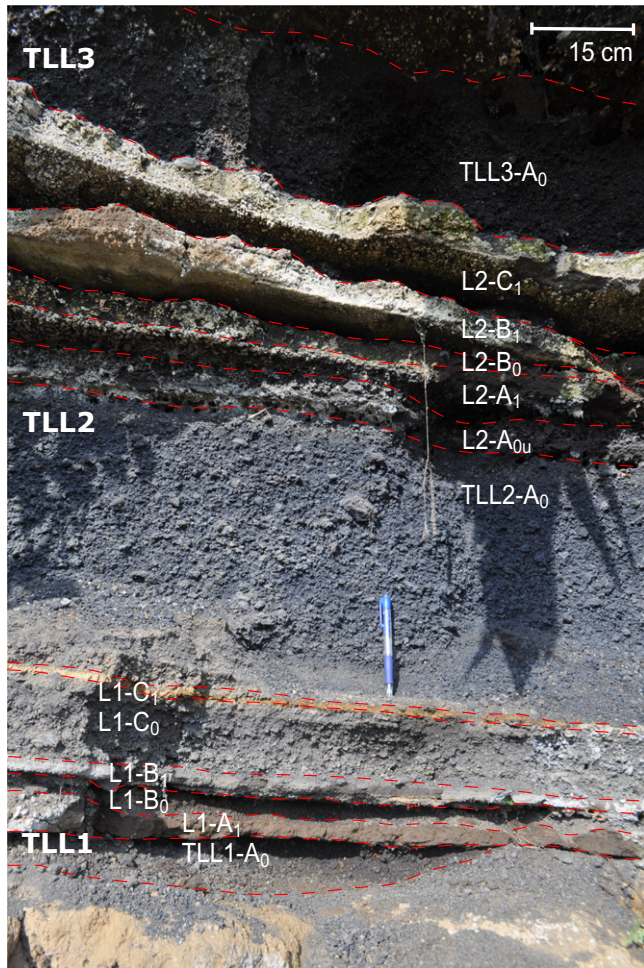
$$N_a = \frac{n_{cry}}{A} \tag{2}$$

Fig. 2. A field photograph of locality MTL-LC-01, showing the alternating fall and tuff sequences characteristic of the Masaya Triple Layer eruption. Each layer begins with a thick scoria and lapilli fall (A_0), succeeded by ash deposits (A_1). The subscript denotes scoria (0) and ash (1) grain sizes. Tuff deposits are easily identified as protruding, tan-coloured beds with planar contacts. TLL1-A_0, TLL2-A_0 and TLL3-A_0 represent scoria beds deposited by the initial stage of the opening and Plinian phases of the eruption (subunits I, II and IV of Pérez et al. (2009).

The calculated mean crystal size (S_m) shows good agreement with the long and short axes of plagioclase crystals measured using ImageJ (Blundy and Cashman, 2008):

$$S_m = \sqrt{\frac{\phi}{N_a}} \tag{3}$$

Volumetric number density (N_v) was then calculated for plagioclase (Couch, 2003):

$$N_v = \frac{N_a}{S_m} \tag{4}$$

Crystal size distributions (CSDs) can be used to determine crystal nucleation events and their crystallisation time (τ). The relationship between crystal population density and crystal length for phenocryst and microlite populations can be used to quantify magma residence times within the chamber and conduit (Marsh, 1988; Marsh, 1998; Higgins, 2000; Higgins, 2002). CSDs were obtained for plagioclase phenocrysts and microlites only, due to the difficulty of segmenting anhedral mafic phases. Plagioclase is the most appropriate phase for understanding shallow and *syn*-eruptive processes, as its crystallisation is sensitive to changes in pressure, temperature and H_2O content (Szramek et al.,

2006; Agostini et al., 2013). We first used CSD*Slice* (Morgan and Jerram, 2006) to apply a stereological correction to the 2D BSE images in order to determine the true 3D crystal habit. Following stereological corrections, we used CSD*Corrections* v1.6 (Higgins, 2000, 2002) to create CSD plots which show the number of crystals per unit length per unit volume (p) for a series of crystal size classes (L). Crystals do not exhibit a preferred orientation, so a fabric was not incorporated into the CSD.

The crystallisation times (τ) of phenocrysts and microlites were calculated from the CSD using the slope produced from the linear regression of p *vs. L* (Marsh, 1988; Cashman and Marsh, 1988; Higgins, 2000; Arzilli et al., 2016) and a range of experimentally derived growth rates for plagioclase (Gt) (Cashman, 1988; Shea and Hammer, 2013; Arzilli et al., 2015; Arzilli et al., 2019):

$$slope = \frac{-1}{Gt\,\tau} \tag{5}$$

Crystallisation times of phenocryst and microlite populations were calculated using four different growth rates. Fast growth rates of 10^{-4} mm s^{-1} and 2×10^{-5} mm s^{-1} are appropriate for decompression-induced microlite crystallisation within the conduit (Arzilli et al., 2019; Arzilli et al., 2015). The slowest growth rate of 10^{-7} mm s^{-1} is more representative of larger phenocrysts crystallising within the magma reservoir (Arzilli et al., 2015). The three growth rates above were obtained from decompression experiments using basaltic melts. We also modelled our data using a growth rate of 10^{-6} mm s^{-1} produced from decompression experiments on basaltic andesites (Shea and Hammer, 2013).

2.3. X-ray fluorescence (XRF)

X-ray fluorescence (XRF) spectrometry was conducted at the University of Manchester using a PANalytical spectrometer, which uses an Rh anode X-ray tube and is configured for geochemical analysis of rocks (Potts and Webb, 1992). Bulk rock compositions were measured with an analytical precision better than 5% for all major elements. Samples were prepared as 15 g pressed powder pellets and subject to loss on ignition (LOI) analysis by heating the pellets to 1000 °C. The secondary standard was USGS reference material BHVO-2 (Wilson, 2000).

2.4. Electron probe microanalysis (EPMA)

We used a JEOL JXA-8530F FEG electron microprobe at the Photon Science Institute, University of Manchester, to determine the major element concentrations of crystal phases, melt inclusions and matrix glasses in seven scoriae samples. Thin sections of scoriae were polished to expose mineral phases, melt inclusions and matrix glass. Melt inclusions are hosted in plagioclase and olivine phenocrysts and are free of visible cracks and bubbles. However, the inclusions are range between 10 and 80 μm in diameter and only inclusions with diameters >30 μm hosted in plagioclase were suitable for EPMA analysis. An acceleration voltage of 15 kV, beam diameter of 1 μm and beam current of 7 nA was used for mineral phases, and a beam condition of 5 μm and 4 nA for glasses to reduce beam damage to the glass. Na and K were measured first to minimise loss by volatilisation, followed by Si, Ca and Fe. Peak counting times varied between 20 and 30 s for most elements, and 50 s for low-concentration elements such as Mn. Calibration standards were jadeite for Na, sanidine for K, wollastonite for Ca, corundum for Al, fayalite for Fe, tephroite for Mn and rutile for Ti. The standard used for Si was fayalite, wollastonite or sanidine, depending on the mineral phase analysed. Analytical uncertainties are 4% for Na_2O, 3% for TiO_2, 2% for K_2O and MgO, 1% for CaO, Al_2O_3, SiO_2 and FeO and 10% for MnO. Data were processed using Probe for EPMA software (v. 12.4.6). Full compositional data for crystal phases and melt inclusions are provided in Supplementary Table 1.

2.5. Raman spectroscopy

H_2O concentrations in melt inclusions were measured using Raman spectroscopy. Raman spectra of glass within melt inclusions hosted in plagioclase and olivine phenocrysts were obtained using a Thermo Scientific DXR xi Raman Imaging Microscope at the School of Earth Sciences, University of Bristol. Samples were prepared as 1-in. rounds, mounted in epoxy resin, and polished in order to expose melt inclusions. Spectra were acquired between 100 cm^{-1} and 4000 cm^{-1} using the 100× objective and a laser power of 3 mW and laser wavelength of 532 nm, at the sample surface and at a depth of 5 µm. To minimise the signal-to-noise ratio, three scans with an exposure time of 10 s were acquired.

We applied the procedure of Long (1977) to correct for temperature and excitation line effects. For the silicate region, a background subtraction was required (Di Genova et al., 2017). For the water region, a cubic baseline was applied between 2750 and 3100 and 3750–3900 cm^{-1}. The water content of the melt inclusions was estimated by calibrating to two well-characterised basaltic glass standards (KR1 and KR2 of Di Genova et al., 2017). The internal calibration method was used to calculate the water content, utilising the ratio between the high wavelength water and low wavelength silicate regions. A root-mean-square error of 0.15% is found for water contents calculated using the internal calibration method (Di Genova et al., 2017).

3. Results

3.1. The La Concepción tephra deposit

We analysed scoria deposits (A_0) from each layer at sample site MTL-LC-01, corresponding to TLL1-A_0, TLL2-A_0 and TLL3-A_0 (Fig. 2). At site MTL-LC-01, TLL1-A_0 is 7.5 cm thick and is a massive, well-sorted, fine-grained black scoria deposit. Scoriae (1 cm) are glassy, have 60 vol% vesicularity, and are found with black lapilli and 2 mm sub-rounded lithic clasts. TLL2-A_0 is 45 cm thick, reverse-graded and poorly sorted, with angular bombs and 0.3–2 cm black sub-angular scoriae and lapilli. Scoriae are glassy and low-density with a higher vesicularity of 85 vol%. TLL3-A_0 is a 25 cm thick, normally graded layer of moderately sorted, 0.3–1 cm black scoriae with 60 vol% vesicularity, lapilli, and 1 cm angular lithic clasts.

3.2. Sample petrography and micro-textural observations

The mineralogical assemblage consists of plagioclase (Plg), clinopyroxene (Cpx), olivine (Ol) and titanomagnetite (Ti-Mag). Scoriae are fine-grained with ~5 vol% plagioclase, ~3 vol% clinopyroxene and ~2 vol% olivine phenocrysts >200 µm in size. The modal proportion of phenocrysts is reported as an average across TLL1, TLL2 and TLL3. The groundmass consists of glass, randomly orientated plagioclase microlites with clinopyroxene overgrowths, and dendritic oxides. There is significant textural variation within individual scoria clasts, with microlite-rich regions containing 50–65 vol% glass (Fig. 3a) and microlite-poor regions containing 75–80 vol% glass (Fig. 3b) (Table 1). Irregular inter-mingling boundaries occur between these distinct textural regions, often defined by cruciform spinel (Fig. 3c, d). This heterogeneity is randomly distributed, and is not found as a systematic textural variation from the core to the rim of the same clast. We can therefore assume that this heterogeneity is not produced by different cooling rates between the slower-cooling core and the quenched rim of the scoria after fragmentation (Szramek et al., 2010). There are textural similarities between the three phases of the eruption, although there are a lesser proportion of microlite-rich zones in TLL1 compared to Plinian phases TLL2 and TLL3. Vesicle texture varies with crystallinity, with microlite-poor regions showing small, spherical and isolated vesicles, whilst microlite-rich regions typically contain irregular, lobate and connected vesicle structures.

Two distinct phases of crystallisation can be identified from the CSD analysis (Fig. 4). We use this to define two distinct crystal size classes: phenocrysts (40–350 µm) and microlites (<40 µm). This division is supported by further textural and chemical evidence, summarised in
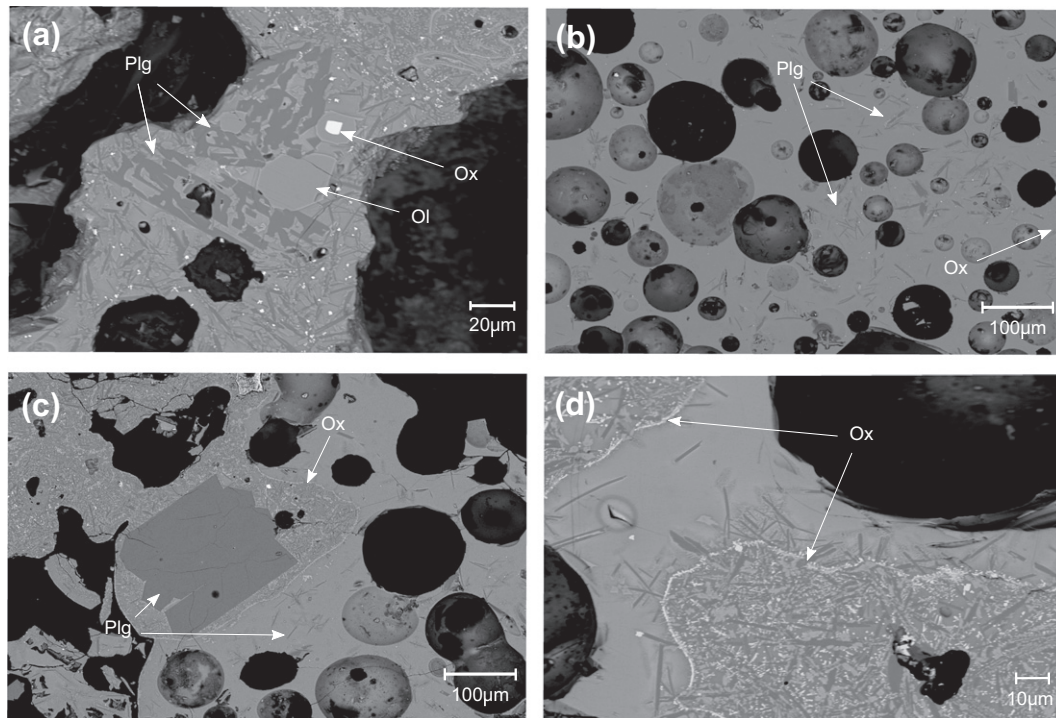

Fig. 3. Back-scattered electron images showing the main textural features of a scoria clast from TLL2. [a] Skeletal plagioclase phenocrysts, within a groundmass assemblage. [b] A microlite-poor region exhibiting spherical, isolated vesicles and hopper plagioclase microlites. [c] Heterogeneous microlite-rich and microlite-poor regions, with an irregular contact defined by oxide crystallisation. A euhedral tabular plagioclase phenocryst is observed in the microlite-rich region. [d] Oxide crystallisation defining the contact between microlite-rich and microlite-poor regions.

Table 1
Crystal fraction (ϕ), number density (N_a), mean crystal size (S_m) and volumetric number density (Nv) for crystal populations in TLL1, TLL2 and TLL3 of the Masaya Triple Layer Eruption. Crystal fraction was calculated using Eq. (1) (Methods). Due to the difficulty in segmenting small, anhedral (<5 μm) mafic phases with comparable contrast, olivine and pyroxene are classified together and calculated from the vesicle-free area of the sample, removing the plagioclase and oxide ϕ. N_a was calculated using Eq. (2), S_m using Eq. (3), and N_v using Eq. (4) for plagioclase.

ϕ	TLL1 (microlite-rich)	TLL1 (microlite-poor)	TLL2 (microlite-rich)	TLL2 (microlite-poor)	TLL3 (microlite-rich)	TLL3 (microlite-poor)
Plagioclase	0.14	0.13	0.21	0.11	0.23	0.1
Olivine + pyroxene	0.21	0.12	0.27	0.09	0.24	0.15
Oxide	0.003	0.002	0.03	0.006	0.01	0.003
Glass	0.65	0.75	0.5	0.8	0.52	0.75
Number density N_a (mm^{-2}) Plagioclase	1.5×10^4	1.3×10^4	5.2×10^4	2.5×10^3	1.7×10^4	5.2×10^3
Mean crystal size S_m (μm) Plagioclase	3	3	2	2	4	1
Volumetric number density N_v (mm^{-3}) Plagioclase	5×10^6	4.1×10^6	2.6×10^7	3.7×10^5	4.6×10^6	1.2×10^6

Section 3.3.2. Plagioclase phenocrysts show euhedral, blocky and rectangular morphologies with higher anorthite contents of An$_{72-89}$. In contrast, microlites show swallowtail and hopper crystal morphologies, tabular and acicular habits, and have lower anorthite contents of An$_{56-68}$. Spherulitic and 'bow-fan' arrangements are common for microlites. Anhedral plagioclases are 100–350 μm in size. The crystal fraction (phenocrysts and microlites) of plagioclase is 0.14–0.13 for TLL1, between 0.21 and 0.11 for TLL2 and 0.23 and 0.1 for TLL3 for microlite-rich and microlite-poor regions respectively. For mafic phases, the crystal fraction is between 0.21 and 0.12 for TLL1, between 0.27 and 0.09 for TLL2 and between 0.24 and 0.15 for TLL3 for microlite-rich and microlite-poor regions respectively. Oxide crystal fraction is lowest in TLL1 between 0.003 and 0.002, ranging between 0.03 and 0.006 for TLL2 and between 0.01 and 0.003 for TLL3. The total crystallinity is between 0.35 and 0.25 for TLL1, ranges between 0.5 and 0.2 for TLL2 and 0.48 and 0.25 for TLL3, for microlite-rich and microlite-poor regions respectively (Table 1).

Phenocrysts and larger microlites of olivine are euhedral and prismatic, between 25 and 100 μm in size. Smaller 1–10 μm microlites of olivine and clinopyroxene have swallowtail to skeletal morphologies. Oxides mainly form dendrites within glass, with rare euhedral to subhedral cubic microlites 10–20 μm in diameter.

CSD analysis finds two slopes for plagioclase crystals (Fig. 4), which correspond to two populations of different size and morphology. Slopes calculated for euhedral, blocky phenocrysts range between −47 and −104.6 mm^{-1} and between −181.7 and −208.2 mm^{-1} for hopper-skeletal microlites. CSD intercepts range between 16 and 17.7 mm^{-4} for phenocrysts and 19 and 20.5 mm^{-4} for microlites. Slopes and intercepts are similar for TLL1, TLL2 and TLL3 (Table 2).

3.3. Phase chemistry

3.3.1. Bulk rock, melt inclusion and glass compositions

Bulk rock, melt inclusion and glass compositions are summarised in Supplementary Table 1. Harker-style diagrams illustrating the evolution of SiO$_2$, MgO, CaO, FeO and K$_2$O from bulk to glass compositions are presented in Fig. 5. The Plinian phases of the Masaya Triple Layer have a basaltic bulk rock composition which ranges between 50.0 and 50.5 wt% SiO$_2$ (Fig. 5). This composition is comparable to that of a previous study, which also determines a basaltic bulk rock composition of 50.2–51.0 wt% SiO$_2$ and 3.5–4.0 wt% alkalis for the Masaya Triple Layer, although the MgO content of our samples is elevated compared to that of Pérez et al. (2009) which find 4.2–4.7 wt% MgO. Plagioclase-hosted melt inclusions are more evolved than the bulk rock and have a basaltic to basaltic andesitic composition of 51–53 wt% SiO$_2$.

Matrix glasses are basaltic andesitic (52–54 wt% SiO$_2$) and are slightly more evolved than the melt inclusion compositions. The decrease in MgO with increasing SiO$_2$ and the scattered distribution of
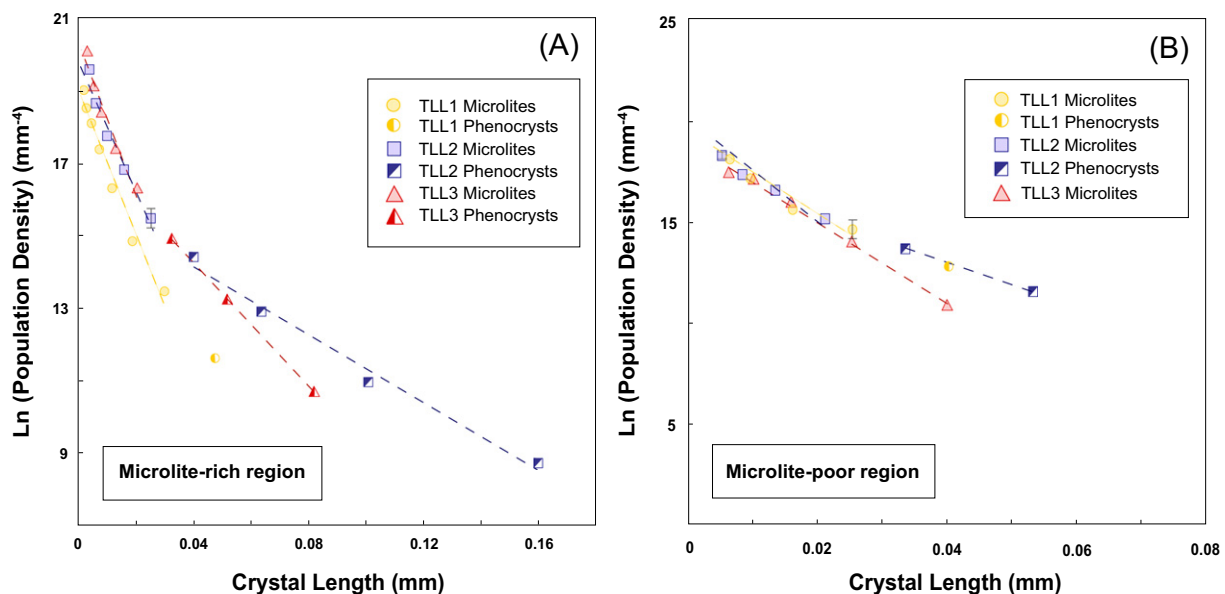

Fig. 4. Crystal size distributions calculated for microlite-rich [a] and microlite-poor [b] regions of the same scoria clast. Microlite and phenocryst populations are evident from the different gradients.

Table 2

A summary of the CSD analysis for TLL1, TLL2 and TLL3, presenting the slopes and intercepts determined from Fig. 4. Experimental growth rates were used to calculate the residence times for microlites (10–40 μm) and phenocrysts (>40 μm) using Eq. (2). Four growth rates were used to produce the minimum (t_r min) and maximum (t_r max) residence times. The growth rates of 10^{-4} and 2×10^{-5} mm s^{-1} are most appropriate for microlites undergoing crystallisation during ascent within the conduit, and the t_r max value is appropriate for phenocrysts crystallising at slower rates within the magma chamber (Shea and Hammer, 2013; Arzilli et al., 2015; Arzilli et al., 2019). CSDSlice used a linear regression to produce the stereographic correction from 2D BSE images to a 3D representation of crystal habit. The R^2 value represents the goodness of fit (Morgan and Jerram, 2006). Lower R^2 values were gained from BSE images with a greater proportion of small (<5 μm) anhedral microlites. Intercepts and slopes were calculated using the CSDCorrections program (Higgins, 2002).

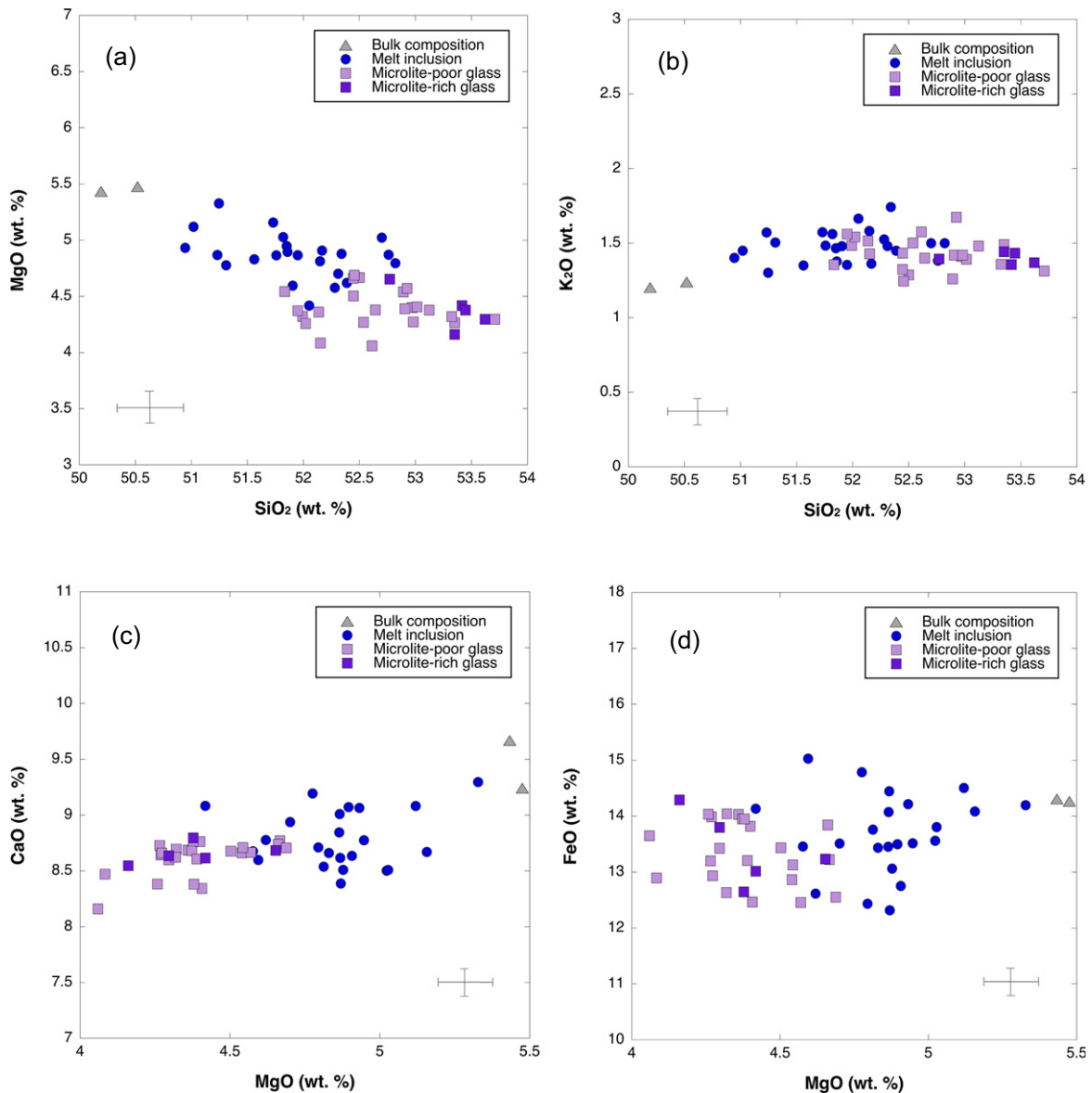| Sample	Intercept (mm^{-4})	Slope (mm^{-1})	t_r min (s)	t_r (m)	t_r (h)	t_r max (h)	t_r max (d)	CSDSlice R^2
TLL1 microlite (microlite-poor)	19.07	−181.71	55	4.59	1.53	15.29		0.87
TLL1 microlite (microlite-rich)	19.05	−190.54	52	4.37	1.33	13.34		0.76
TLL2 phenocryst (microlite-rich)	16.04	−46.98	213	17.74	5.91		2.46	0.59
TLL2 microlite (microlite-rich)	19.93	−183.86	54	4.53	1.51	15.12		
TLL2 phenocryst (microlite-poor)	17.17	−104.57	96	7.97	3.26		1.36	0.71
TLL2 microlite (microlite-poor)	19.18	−191.73	39	3.21	1.33	13.34		
TLL3 phenocryst (microlite-rich)	17.67	−85.09	118	9.79	3.26		1.36	0.68
TLL3 microlite (microlite-rich)	20.54	−208.2	48	4	1.33	13.34		
TLL3 microlite (microlite-poor)	18.98	−199.54	50	4.18	1.39	13.92		0.87
Experimental growth rates			Ar2019 (mm s^{-1}) 1.E−04	Ar2015 (mm s^{-1}) 2.E−05	SH2013 (mm s^{-1}) 1.E−06	Ar2015 (mm s^{-1}) 1.E−07		

Fig. 5. Major element plots of bulk rocks, melt inclusions and matrix glasses from the Masaya Triple Layer eruption. Bulk rock compositions were measured by XRF; melt inclusion and glass compositions were measured by EPMA. All data are normalised to anhydrous compositions. Error bars show 1σ uncertainty for EPMA data.

FeO in melt inclusions and glass may be controlled by clinopyroxene and olivine crystallisation (Fig. 5a, d). The non-linear FeO distribution may also depend on the heterogeneous crystallinity of the sample. K_2O is relatively constant between melt inclusions and glass, as K_2O is incompatible with crystallising phases (Fig. 5b). CaO decreases with decreasing MgO (Fig. 5c), due to the compatibility of CaO in plagioclase and clinopyroxene. We observe a small degree of differentiation from melt inclusions to glass, with generally more evolved glass compositions measured in microlite-rich regions. As melt inclusions are likely to be trapped at different stages of melt evolution, some of their compositions slightly overlap with the less evolved, microlite-poor glass regions.

3.3.2. Chemistry of crystal phases

Plagioclase phenocrysts are typically unzoned in TLL2 and TLL3, but a few crystals have more anorthitic cores and more albitic rims. However, 100–350 μm euhedral phenocrysts from TLL1 show a continuous range of compositions between 64 and 82 mol% An. Phenocryst rims have a range in anorthite content of 64–73 mol%, which overlaps that of microlites and skeletal phenocrysts in TLL1. Furthermore, there is an apparent shift in the An content of phenocryst rims, from the more albitic rims of TLL1 to the An-rich rims of TLL2 and TLL3. Phenocrysts in TLL2 and TLL3 show a narrower range of more anorthitic compositions, with little variation between cores and rims. In addition, plagioclase chemistry varies between populations across TLL1, TLL2 and TLL3 (Fig. 6). Phenocryst cores have higher An content between 73

and 89 mol% and are distinct from the more albitic microlite population. Microlites in TLL2 and TLL3 are characterised by An content between 56 and 65 mol%. Skeletal phenocrysts have the largest compositional range, between 59 and 74 mol% An.

Olivine phenocrysts and microlites are compositionally homogenous and unzoned. Forsterite content varies between 70.7 and 72.4 mol% for phenocrysts and microlites of TLL1, TLL2 and TLL3 (Fig. 7a). Clinopyroxene phenocrysts and microlites are augitic to diopsidic (En_{41-47}, Fs_{11-19}, Wo_{36-45}) (Fig. 7b). Magnetitic oxide microlites contain 5.9–7.1 wt% TiO_2, 3.4–4.3 wt% MgO and 4.9–6.2 wt% Al_2O_3. Mineral compositions are provided in Supplementary Table 1.

3.3.3. H_2O concentrations in melt inclusions

Due to the rarity of phenocrysts and consequently melt inclusions in samples of the Masaya Triple Layer eruption, Raman spectra were obtained from inclusions trapped within five olivine phenocrysts. Spectra produced from the measurement of plagioclase-hosted melt inclusions had low signal-to-noise ratios and so were excluded from further analysis. Spectra with a high signal-to-noise ratio of melt inclusions showing no evidence of post-entrapment crystallisation were selected to quantify H_2O concentrations. H_2O concentrations are relatively uniform between eruptive phases (Fig. 8), within the analytical uncertainty of the measurements. The maximum H_2O content of 2 wt% was measured in a melt inclusion from Plinian phase TLL3. For TLL1, H_2O concentrations range between 1.3 and 1.5 wt% (Fig. 8).
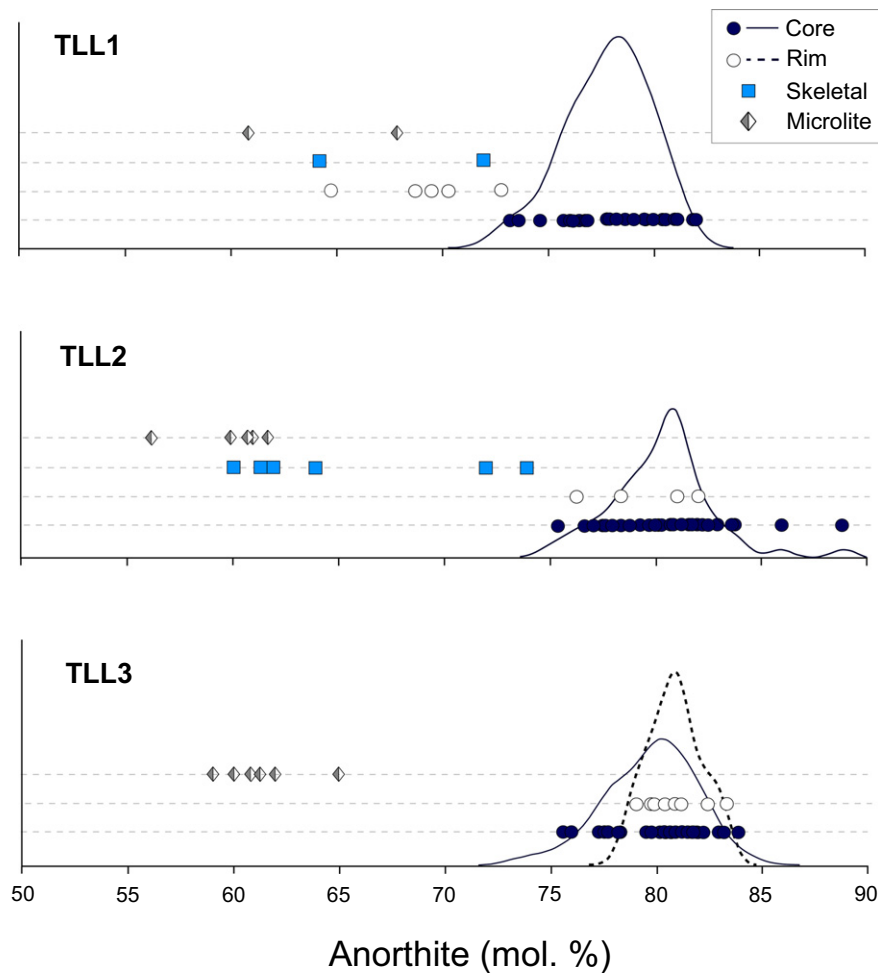

Fig. 6. Anorthite mol.% for plagioclase phenocrysts, microlites and skeletal phenocrysts in samples from TLL1, TLL2 and TLL3. Kernel density distributions are plotted for phenocryst cores in TLL1 and TLL2, and for both phenocryst cores (solid lines) and rims (dashed lines) in TLL3.
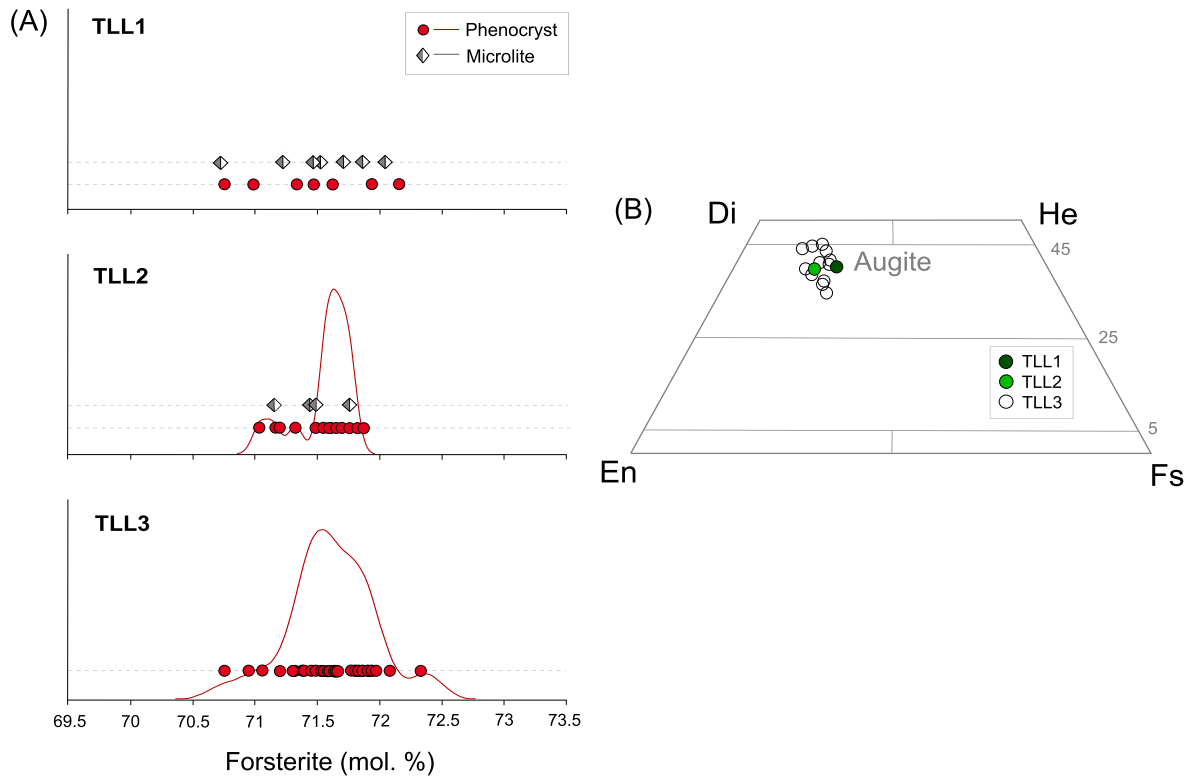
Fig. 7. (a) Forsterite mol.% for olivine phenocrysts and microlites in samples from TLL1, TLL2 and TLL3. Kernel density distributions are plotted for phenocrysts in TLL2 and TLL3. (b) Clinopyroxene phenocryst compositions in samples from TLL1, TLL2 and TLL3.
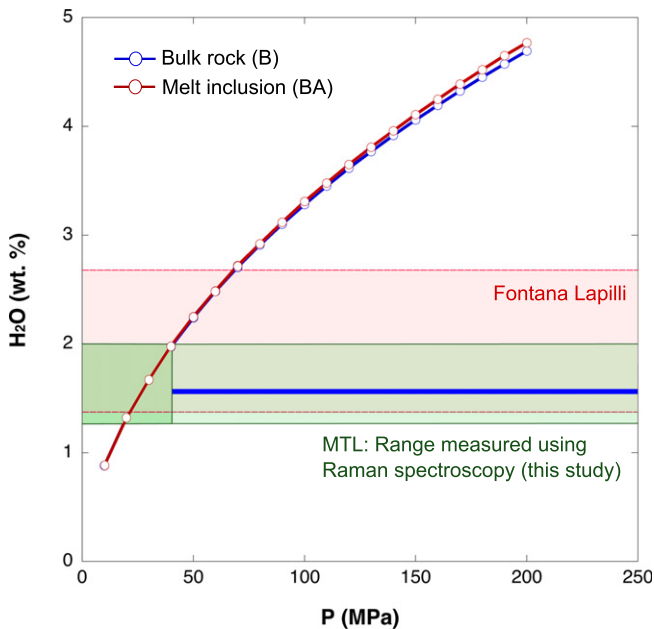
4. Discussion

4.1. Pre-eruptive conditions

To determine the pressure and temperature of phenocryst crystallisation and thereby understand the pre-eruptive magmatic storage conditions, plagioclase and clinopyroxene EPMA data were incorporated into the mineral-melt thermometers of Putirka (2008). Equation 33 of Putirka (2008) was selected for clinopyroxene, whilst Equations 23 and 24a of Putirka (2008) were compared for plagioclase. Thermometry values and tests for equilibrium are detailed in Supplementary Table 2.

The clinopyroxene thermometer was tested for equilibrium using the average bulk rock, melt inclusion and matrix glass compositions and the criterion $K_D = 0.28 \pm 0.08$ (Putirka, 2008). The majority of clinopyroxene phenocrysts in TLL3 are in equilibrium only with the average melt inclusion composition, producing a temperature range of 1044–1097 °C. Clinopyroxene is rare in TLL1 and TLL2 and so was not used with this thermometer. We can suggest that clinopyroxene crystallisation occurred between 1044 and 1097 ± 45 °C (Fig. 9).

For plagioclase, the mineral-melt thermometers (Putirka, 2008) were tested for equilibrium using the average bulk rock, melt inclusion and matrix glass composition, using the criterion $K_D = 0.28 \pm 0.11$. Phenocrysts, microlites and skeletal plagioclase were mostly found to be in equilibrium with the average melt inclusion composition. Results and tests for equilibrium are detailed in Supplementary Table 2. Similar crystallisation temperatures were calculated for TLL1, TLL2 and TLL3 but vary according with plagioclase crystal morphology (Fig. 9). As Equation 24a is the more precise mineral-melt thermometer, with a lower standard error of ±36 °C, the results of this thermometer are described here (Putirka, 2008). Phenocryst cores in TLL2 and TLL3 have the highest temperature range, between 1090 and 1092 °C. In TLL1, phenocryst cores crystallised over a lower temperature range of

Fig. 8. Results of the Moore et al. (1998) solubility model for H_2O (wt%) with pressure (MPa), using both averaged bulk rock (basalt - B) and melt inclusion (basaltic andesite - BA) compositions. The range of H_2O concentrations measured in melt inclusions using Raman spectroscopy is shaded in green. H_2O measured in melt inclusions of the Fontana Lapilli Plinian eruption are shown in red (Sadofsky et al., 2008; Goepfert and Gardner, 2010; Wehrmann et al., 2011). The maximum H_2O concentration measured in tephra samples of Masaya's more recent, low-explosive activity is shown by the blue bar (Zurek et al., 2019).
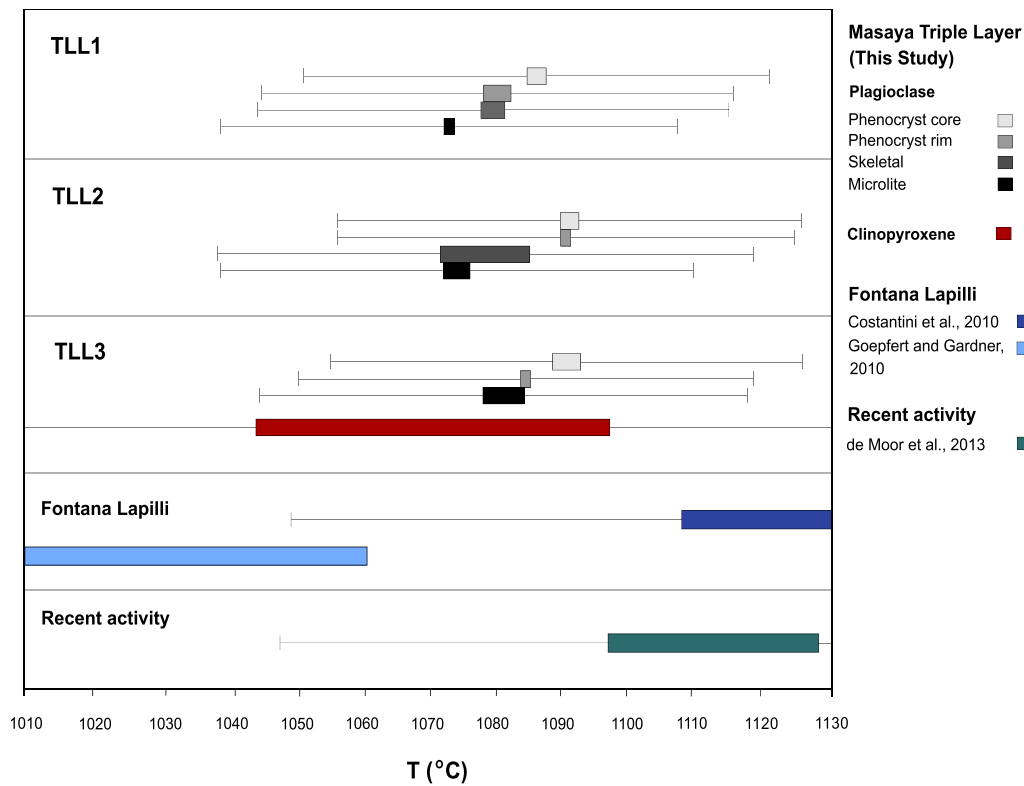
Fig. 9. A summary of the temperature ranges calculated using the Putirka (2008) mineral-melt thermometers for plagioclase and clinopyroxene. Plagioclase crystallisation temperatures are subdivided by crystal type. The 2 sigma uncertainty associated with each thermometer is expressed as a bar. Literature data illustrating the difference in temperature for the Fontana Lapilli eruption (Costantini et al., 2010) and for scoriae of recent activity at Masaya (de Moor et al., 2013), are highlighted in blue and green respectively.

1086–1087 °C, suggesting crystallisation conditions differed for phenocrysts in TLL1. More albitic phenocryst rims in TLL1 crystallised over a lower and wider temperature range of 1077–1083 °C. This range is comparable with the temperature range of equilibration for microlites of 1073–1083 °C and skeletal phenocrysts of 1065–1084 °C.

We used Rhyolite-MELTS v. 1.2 (Gualda et al., 2012) to constrain the pressure conditions of phenocryst crystallisation, following the method of Arzilli et al. (2019b). Rhyolite-MELTS was first used to construct a phase diagram for the Masaya Triple Layer bulk rock composition by running a series of simulations between 10 and 100 MPa assuming water-saturated conditions (Fig. 10). The water concentration at saturation for each pressure interval was determined using the H_2O solubility model of Moore et al. (1998) (Fig. 8). The initial H_2O concentration was then adjusted in accordance with the starting pressure of the simulation, in order to maintain water saturation of the melt. We produced Rhyolite-MELTS simulations using the oxygen fugacities of NNO, NNO–0.65 and NNO + 1.35. This range is in accordance with the experimental phase diagram of the Fontana Lapilli eruption, which is fixed at the NNO buffer (Goepfert and Gardner, 2010). The simulations run at NNO yield crystallising assemblages that are most consistent with the observed crystal assemblage in our Masaya Triple Layer samples (Supplementary Table 3). Results from the NNO-0.65 simulations do not match the observed assemblage: under these reducing conditions the simulations predict a higher proportion of more fayalitic olivine where Fo# < 71.5, which is not consistent with the narrow range in forsterite number measured in our samples (Fig. 7a). The NNO + 1.35 simulations predict an olivine-absent mineral assemblage, which does not match our olivine-bearing samples.

The pre-eruptive condition was constrained by comparing the simulated phenocryst crystal fraction at a series of P-T intervals with the measured phenocryst ϕ from textural analysis of natural scoriae samples. We exclude the microlite ϕ as we assume their crystallisation

occurs during magma ascent and is not representative of the pre-eruptive condition. The P-T window where both the natural ϕ and assemblage of plagioclase, clinopyroxene and olivine corresponded to the simulation output was selected as the probable condition of phenocryst crystallisation. A summary of the Rhyolite-MELTS simulations is provided in Supplementary Table 3. The P-T window of 21–42 MPa and 1080–1100 °C most closely matches the observed low phenocryst ϕ for plagioclase (~5 vol%), clinopyroxene (~3 vol%) and olivine (~2 vol%) for our samples (Fig. 10). Higher storage pressures predict an olivine-absent assemblage with a considerably higher clinopyroxene ϕ relative to plagioclase. Lower pressures do not accurately reproduce our observed modal proportions of clinopyroxene and plagioclase. The P-T conditions determined from the Rhyolite-MELTS simulations are also consistent with the temperature ranges of equilibration defined by clinopyroxene and plagioclase thermometry, when accounting for the uncertainty of the thermometers.

Thermometric calculations and Rhyolite-MELTS simulations indicate a small phenocryst crystal fraction was able to crystallise under water-saturated conditions, within a magma reservoir at low pressures between 21 and 42 MPa and therefore, at shallow depths of 0.8–1.6 km. Due to the measured maximum H_2O concentration of 2 wt%, the magma reservoir is more likely to be situated at a pressure of 42 MPa and a depth of 1.6 km (Fig. 8). This depth range is consistent with the ~1 km depth inferred for the shallow crustal magma reservoir of the current Masaya caldera system, constrained by microgravity surveys and epicentres of volcano-tectonic earthquakes (Williams-Jones et al., 2003; Métaxian et al., 1997). Seismic tomography finds that a low velocity anomaly is currently present at depths of 0-3 km beneath Masaya caldera, but no evidence of a magma plumbing system at greater depth (Obermann et al., 2019). Although Bouguer gravity surveying and seismic tomography find a dense body at depths of 3-8 km, this body may represent an intrusion emplaced prior to caldera collapse,
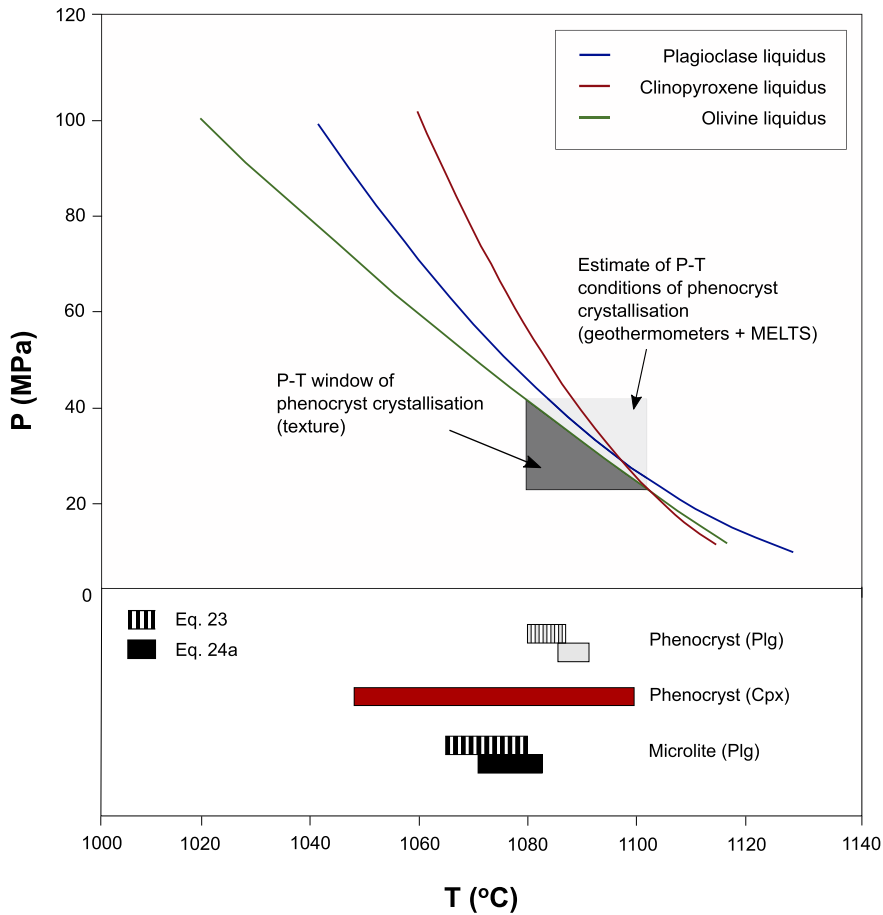
Fig. 10. The phase diagram constructed for the Masaya Triple Layer average bulk composition using Rhyolite-MELTS, assuming oxygen fugacity at the NNO buffer. The liquidii of plagioclase, olivine and clinopyroxene are indicated. By combining the results of mineral-melt thermometers and Rhyolite-MELTS we can estimate the P-T conditions of phenocryst crystallisation, highlighted in grey. Then by comparing these results with the measured crystal fraction we can constrain the P-T window which may have produced the crystal assemblage observed in samples. Results of the Putirka (2008) mineral-melt thermometers show the expected ΔT for plagioclase and pyroxene phenocrysts and microlites. For plagioclase, calculated temperatures from equations 23 and 24a of Putirka (2008) are shown as dashed and solid boxes respectively.

as the morphology of the anomaly is not consistent with the current caldera structure (Métaxian, 1994; Obermann et al., 2019). The increased FeO and CaO/Al$_2$O$_3$ of Masaya lavas relative to basalts of the Nicaraguan arc with plagioclase as the main phenocryst phase, is suggestive of fractional crystallisation at low pressure and at low magmatic H$_2$O (Grove and Baker, 1984; Walker, 1989; Walker et al., 1993). Conversely, a calc-alkaline trend would be produced by fractional crystallisation at higher pressure and higher magmatic H$_2$O, with an increased proportion of olivine and clinopyroxene (Grove and Baker, 1984; Walker et al., 1993). The tholeiitic composition of the Masaya lavas, and tectonic setting of the volcano, can be explained by the localised thinner crust of Nicaragua with respect to the Central American Volcanic Arc (Walker, 1989; Walker et al., 1993).

Masaya lavas show chemical homogeneity both prior to and following caldera formation (Walker et al., 1993; Zurek et al., 2019). Although the current structure of Masaya Volcano reflects the low explosive activity which has occurred following formation of the caldera, this compositional homogeneity of erupted magmas suggests a comparable subsurface system through time. Therefore, the structure of Masaya caldera, geophysical surveying of its current reservoir, and the eruptive history of Masaya, suggest that the magma of the Masaya Triple Layer was last stored at shallow depth prior to eruption. This depth can also explain the frequent alternation between Plinian magmatic and phreatomagmatic activity during the eruption (Pérez et al., 2009). At shallow depths of 0.8–1.6 km, water could access the conduit, inducing frequent, potentially intense phreatomagmatic explosions and column collapse (Pérez et al., 2009; Swanson et al., 2012).

4.2. Syn-eruptive conditions

4.2.1. Timescales of crystallisation

We calculated the residence times of plagioclase microlites within the conduit by incorporating the CSD analyses and experimentally determined plagioclase growth rates into Eq. (5). We used a representative range of experimental growth rates between 10^{-4} mm s^{-1} and 10^{-7} mm s^{-1} (Arzilli et al., 2019; Arzilli et al., 2015; Shea and Hammer, 2013) to calculate minimum and maximum residence times. These growth rates were determined from decompression experiments with bulk compositions, degrees of water saturation and degrees of undercooling (Agostini et al., 2013; Arzilli et al., 2015; Shea and Hammer, 2013; Arzilli et al., 2019) that closely match the Masaya Triple Layer. The decompression experiments were saturated with 0.6–2.3 wt % H$_2$O, depending on the starting pressure (Agostini et al., 2013; Arzilli et al., 2015). The experimental pressure range of 5–50 MPa is comparable with our melt inclusion H$_2$O concentrations, the range of pre- and syn-eruptive conditions calculated using Rhyolite-MELTS and the solubility model of Moore et al. (1998) as applied to the Masaya Triple Layer bulk composition (Fig. 8). To estimate the residence time of phenocrysts in the magma reservoir we use a plagioclase growth rate of 10^{-7} mm s^{-1} obtained at conditions of 50 MPa, 2.34 wt% H$_2$O and at low undercooling. The growth rate of 2×10^{-5} mm s^{-1}, obtained at conditions of 5 MPa, 0.6 wt% H$_2$O and high undercooling, was used as a representative growth rate for microlites in the conduit (Agostini et al., 2013; Arzilli et al., 2015). The growth rate of 10^{-4} mm s^{-1}, obtained through experiments which induced a rapid increase of

undercooling, was used to constrain minimum residence times of microlites within the conduit, as these conditions are likely representative of the fast magma ascent expected during highly explosive basaltic eruptions (Arzilli et al., 2019).

Assuming microlite crystallisation is induced by decompression during magma ascent along the conduit, from the magma chamber to the surface, we can suggest a rapid ascent time for the Masaya Triple Layer magma. Our calculated crystal residence times suggest that microlites were able to crystallise within 1–5 min (Table 2). Longer crystallisation timescales of 13 to 15 h are likely to be more representative of phenocryst growth within the magma chamber at low undercooling. Tabular-prismatic plagioclase phenocryst morphologies are likely to result from relatively slow growth rates of 10^{-7} mm s^{-1}, whilst hopper-skeletal plagioclases are likely to be produced at faster growth rates between 10^{-4} mm s^{-1} and 2×10^{-5} mm s^{-1} (Agostini et al., 2013; Arzilli et al., 2015; Arzilli et al., 2019). Heterogeneous clinopyroxene crystallisation upon plagioclase also has a fast growth rate of 10^{-4} mm s^{-1} (Arzilli et al., 2019). *In situ* 4D crystallisation experiments demonstrate that crystallisation with large undercooling can be exceptionally rapid, within a few minutes. This timescale of crystallisation is compatible with the fast magma ascent simulated by numerical models of the 1886 Tarawera and Etna 122 BCE basaltic Plinian eruptions, which predict ascent times of <10 min prior to magma fragmentation (Moitra et al., 2018; Arzilli et al., 2019; Campagnola et al., 2016). A residence time of hours to days exceeds the simulated magma ascent rate for basaltic Plinian eruptions (Moitra et al., 2018; Campagnola et al., 2016; Szramek, 2016).

The inflected CSD slopes observed for each layer reflect a temporal change in nucleation rate, and ultimately the decompression and cooling rate controlling crystallisation (Marsh, 1988; Marsh, 1998). CSD slopes of the Masaya Triple Layer are comparable with those of the 2.2 ka Yufune-2 basaltic sub-Plinian eruption of Fuji (Suzuki and Fujii, 2010). However, these slopes are two orders of magnitude larger than CSDs of scoriae at Stromboli. Eruptions of lower explosivity than the Plinian Masaya Triple Layer eruption, such as the August 1998 paroxysm and July 1994–September 1996 period, show average slopes of −4.45 and −7.62 respectively (Armienti et al., 2007; Fornaciai et al., 2009). Comparison of CSDs of the Masaya Triple Layer eruption with those of Strombolian activity indicates that it is the rapidity of this crystallisation that is distinctive for basaltic sub-Plinian to Plinian activity. High volumetric number densities of 4.6×10^6 mm^{-3}–2.6×10^7 mm^{-3} are observed for microlite-rich domains of TLL2 and TLL3 and exceed that of sub-Plinian eruptions by an order of magnitude (Suzuki and Fujii, 2010). Significant microlite crystallinity is observed in scoriae from several basaltic Plinian eruptions such as the Fontana Lapilli, the 122 BCE Etna eruption and 1886 Tarawera eruption, where the maximum crystallinity can vary between 64 and 99 vol% (Sable et al., 2006; Costantini et al., 2009; Sable et al., 2009). Therefore, rapid and substantial microlite crystallisation over 1–5 min likely produced significant changes in viscosity and magma rheology within the conduit during ascent, increasing the likelihood of magma fragmentation (Sable et al., 2006; Sable et al., 2009; Moitra et al., 2018).

The difference in phenocryst compositions between TLL1 and TLL2-TLL3 could suggest crystallisation conditions differed between the opening and Plinian phases of the eruption. The more albitic rims of phenocrysts in TLL1 could reflect a more prolonged interaction with a more evolved carrier melt, during crystallisation of microlites and skeletal phenocrysts with comparable albite content. Phenocrysts with an albitic rim occur within the crystal-rich domain of TLL1, where there is a prevalence of pyroxene and plagioclase microlites. It is possible that, during the opening phase of the eruption, phenocryst rims were able to react with a more evolved carrier melt during initial decompression.

4.2.2. Crystal morphology and undercooling
Effective undercooling (ΔT), the difference between the liquidus temperature and pressure of a phase (T_{liq}) and the temperature and

pressure of its crystallisation ($\Delta T = T_{liq}$-T), provides the driving force for crystallisation and controls the evolution of texture through time. Crystal growth dominates at small $\Delta T/\Delta t$ (where t is equivalent to time), producing an assemblage of coarse-grained euhedral crystals with low volumetric number density (N_v), whilst high $\Delta T/\Delta t$ favours nucleation, enabling rapid growth of numerous hopper-skeletal crystals with high N_v (Hammer and Rutherford, 2002; Shea and Hammer, 2013). We suggest that microlites formed by decompression-induced crystallisation within the conduit during ascent, due to the lower anorthite content of plagioclase microlites compared to phenocrysts (Fig. 6) (Szramek et al., 2006; Agostini et al., 2013; Shea and Hammer, 2013), the crystallisation timescale derived from the CSD analysis, and the dominance of plagioclase N_v with respect to clinopyroxene and olivine (Table 1). The high ϕ of clinopyroxene microlites indicates a high nucleation rate at large ΔT, which is observed only for decompression-induced crystallisation experiments (Shea and Hammer, 2013).

Diffusion-limited microlite crystallisation produced swallowtail and skeletal forms, as crystal growth was restricted by the slow diffusivity of chemical components relative to large ΔT (Lofgren, 1974; Lofgren, 1980). Diffusion-limited growth textures are often observed in magmas with lower dissolved H_2O contents, due to the lower diffusivity of chemical components within dry melts (Shea and Hammer, 2013). Isothermal crystallisation experiments on mid-ocean ridge basalts (Lofgren, 1974; Lofgren, 1980) find that ΔT between 20 and 75 °C produces a transition from acicular to dendritic and spherulitic plagioclase morphologies, whilst prismatic shapes crystallise at $\Delta T < 30$ °C. A similar transition in plagioclase morphology with increasing ΔT is observed for decompression induced crystallisation experiments (Hammer and Rutherford, 2002). Above ΔT values of 75–90 °C, plagioclase and pyroxene spherulites co-exist (Lofgren, 1974). Pyroxene crystallisation experiments performed *via in situ* 4D synchrotron X-ray microtomography in basaltic melts show that pyroxene crystals are dominantly prismatic at $\Delta T = 38$ °C and their habits change from elongate to dendritic as ΔT increases (Polacci et al., 2018). Hopper, skeletal and dendritic microlite morphologies suggest that ΔT for the Masaya Triple Layer was likely between 30 and 70 °C, with crystallisation of radial and bow-fan spherulites at higher $\Delta T > 75$ °C (Lofgren, 1974; Lofgren, 1980). Using our phase diagram (Fig. 10), we can make an estimate of ΔT using the results of the mineral-melt thermometry for microlites. Assuming microlites crystallised at a lower pressure than phenocrysts of <21 MPa, we can suggest that ΔT reaches a maximum of approximately 54–61 °C at 10 MPa, where ΔT is consistent with the microlite morphologies observed (Fig. 10).

At high decompression rates during magma ascent, ΔT is large, producing skeletal microlite morphologies. The equilibrium plagioclase modal proportion is reached in <2 h; therefore, microlite crystallisation likely proceeded under disequilibrium conditions at large ΔT (Arzilli et al., 2015; La Spina et al., 2016). Decompression experiments find decompression rates of 0.1–0.2 MPa s^{-1} for the Fontana Lapilli eruption, which exceed that of silicic Plinian eruptions at 0.01–0.001 MPa s^{-1} (Szramek, 2016) and are consistent with the fast ascent rates proposed for basaltic Plinian eruptions (Sable et al., 2006; Sable et al., 2009; Costantini et al., 2010; Moitra et al., 2018)

4.2.3. Rheological evolution during ascent
We used the rheological models developed by Giordano et al. (2008) and Vona et al. (2011) to investigate the effect of crystallisation upon relative magma viscosity during ascent. The crystal-free melt viscosity is 30–40 Pa s, calculated using the temperature range from thermometers of 1080–1100 °C for the bulk rock composition (Giordano et al., 2008). However, using the crystal content determined from the textural analysis, the relative viscosity increases from 10^2 to 10^6 Pa s as crystal volume fraction increases from 0.2 to 0.5 (Table 1). When crystal volume fraction starts to approach the maximum crystal packing fraction (ϕ_m=0.56), (Costa et al., 2009; Vona et al., 2011; Moitra et al., 2018) magma viscosity reaches the brittle fragmentation threshold of

10^6 Pa s (Papale, 1999). The calculated viscosity varies little with changes in melt temperature and H_2O concentration when compared with changing crystal content, indicating that *syn*-eruptive crystallisation is a dominant control and significant contributor to increased explosivity (Vona et al., 2011).

An increase in viscosity over five orders of magnitude would induce a significant change in magma rheology during ascent. Oscillatory and extensional rheometry comparing both particle-free and particle-enriched suspensions analogous to the Etna 122 BCE and Tarawera magmas finds brittle failure occurs only in the latter case, when strain rates exceed $1\ s^{-1}$ (Moitra et al., 2018). Crystallisation is expected to induce a change from 10^2 Pa s to 10^7 Pa s as crystal fraction approaches the maximum packing fraction (Moitra et al., 2018). The relationship between viscosity and crystal fraction is highly non-linear at large crystal fractions, due to the onset of viscoelastic behaviour as particle interactions increase when approaching ϕ_m (Moitra et al., 2018). Increasing the crystal fraction of the Masaya Triple Layer from 0.2 to 0.5 can produce an increase in viscosity from 10^2 to 10^6 Pa s. The rheological change induced by rapid syn-eruptive crystallisation likely promoted magma fragmentation (Arzilli et al., 2019), contributing to the increased explosivity of the Masaya Triple Layer Plinian eruption.

4.3. Comparing conditions of explosive basaltic activity

4.3.1. Pre-eruptive conditions of Masaya Volcano

The chemical compositions of melt inclusions and crystal phases between the Plinian phases TLL2 and TLL3 are similar, producing a comparable P-T range of crystallisation from thermometry and Rhyolite-MELTS simulations. The similar N_v and calculated residence times for TLL2 and TLL3 also indicate comparable syn-eruptive conditions. This similarity suggests a stable condition for the reservoir of the Masaya Triple Layer eruption, favouring recurrent highly explosive activity. Whilst our conclusions represent the observed textural and compositional heterogeneity in the TLL1, TLL2 and TLL3 layers in a single sample site of the La Concepción facies, we recognise that there are some limitations in generalising these conclusions to the distal facies of the Masaya Triple Layer sequence. Nevertheless, the bulk compositional homogeneity of the Masaya Triple Layer deposit (Pérez et al., 2009) suggests that it is reasonable to infer that the eruption dynamics inferred from our sample set are representative of the entire eruption.

From micro-textural observations we suggest that TLL1 erupted explosively, with a similar mechanism to the Plinian phases of the eruption, but was a lower-intensity sub-Plinian eruption. Importantly, this observation may suggest that there are similar eruptive mechanisms for explosive sub-Plinian to Plinian basaltic volcanism, which are distinct from that of Hawaiian and Strombolian activity where gas-melt separation is facilitated by lower magma viscosity (Parfitt, 2004).

Our data suggest that the Masaya Triple Layer magma was last stored containing a maximum H_2O concentration of 2 wt%, crystallising a small phenocryst fraction in water-saturated conditions. Although this pre-eruptive dissolved H_2O concentration is low compared to other explosive basaltic volcanoes of the Central American Volcanic Arc such as Cerro Negro (VEI 3; 4.8–5.2 wt% H_2O) and Fuego (VEI 4; 4.14 wt% H_2O), there may have been an exsolved H_2O phase, due to the low pressure of phenocryst crystallisation (Sadofsky et al., 2008; Lloyd et al., 2013). Our measurements are comparable with both the pre-eruptive H_2O budget of 0.91–2.7 wt% measured for the Fontana Lapilli basaltic Plinian eruption using SIMS and FTIR (Sadofsky et al., 2008; Goepfert and Gardner, 2010; Wehrmann et al., 2011) and the maximum pre-eruptive H_2O content of 1.45 wt% determined by Raman spectroscopy on recent low-explosive products at Masaya (Zurek et al., 2019).

The consistent low H_2O concentration of eruptive products over 60,000 years, across the explosive-effusive transition of the Masaya caldera complex, suggests either that the degassing path or decompression rate may have as much impact upon explosivity as the initial H_2O budget, or that there is also a contribution from CO_2 (Costantini et al., 2010;

Goepfert and Gardner, 2010; Zurek et al., 2019; Barth et al., 2019). Yet, we find no evidence of carbonate interaction at Masaya such as entrained carbonate xenoliths or carbonate minerals present within the groundmass, which would be suggestive of carbonate assimilation (Allard, 2010; Aiuppa et al., 2011; Blundy et al., 2010; Dallai et al., 2011; Freda et al., 2011; Cross et al., 2014). This is consistent with previous studies of the Masaya deposits (Costantini et al., 2010; Zurek et al., 2019). The majority of the magmatic CO_2 is expected to have exsolved at depth before the magma reached the shallow storage chamber prior to eruption, although CO_2 exsolution could have accelerated magma ascent (Sable et al., 2006; Costantini et al., 2010). However, the current paucity of CO_2 data for Masaya magmas (Wehrmann et al., 2011) means that it is difficult to constrain the CO_2 budget or its degassing path for its basaltic Plinian eruptions.

Crystal phases and bulk compositions of the Masaya Triple Layer samples are consistent with that of Masaya's dominantly effusive activity since 1772, indicative of a long-lived system at Masaya which has exhibited minimal chemical variation through time (Walker et al., 1993; Zurek et al., 2019). Scoriae from basaltic Plinian eruptions and recent activity at the Masaya caldera complex show a similar phenocryst assemblage, with a low crystal fraction of <10 vol%, dominated by plagioclase, with minor amounts of clinopyroxene and olivine (Pérez et al., 2009; Costantini et al., 2010; Goepfert and Gardner, 2010; Zurek et al., 2019). However, explosive-effusive transitions have been observed at several volcanic systems which exhibit geochemical homogeneity through time. Highly explosive activity can be triggered by a magma injection of similar composition, but efficient mixing and homogenisation of the magma within the shallow plumbing system can produce a homogeneous and hybridised composition over several eruptions (Mangler et al., 2019). Explosive paroxysmal activity at Stromboli has been suggested to result from the introduction of volatile-rich, crystal poor (<10 vol%) magma from depth into the shallow feeding system, where it mixes with more degassed, crystal-rich (~50 vol%) magma, evidenced by intricate micron-scale mingling textures between the two end-member magmas (La Felice and Landi, 2011). Both end-members are of comparable composition, but with different viscosity, enabling their mingling and consequent destabilisation of the shallow reservoir, producing an explosive paroxysm (La Felice and Landi, 2011). Despite the chemical homogeneity of the Masaya system, our samples preserve evidence of mingling (Fig. 3c, d). Therefore, we cannot exclude the possibility of magma injection and mixing as a trigger of highly explosive Plinian activity (Walker et al., 1993; La Felice and Landi, 2011; Mangler et al., 2019). To investigate the triggering mechanism in greater detail, further geochemical or microtextural analyses are required.

The cause of the explosive transformation of Masaya Volcano is still enigmatic. A possible contributing factor may be the lower pre-eruptive temperature of the Masaya Triple Layer magma, as compared to the 1097–1127 °C range observed for Masaya's recent activity (de Moor et al., 2013) (Fig. 9). A lower pre-eruptive temperature would produce a larger ΔT, reflected in the skeletal microlite morphologies of the highly crystallised Masaya Triple Layer scoriae. Rhyolite-MELTS simulations comparing the Masaya Triple Layer and Fontana Lapilli eruptions provide a comparison of the pre-eruptive condition of basaltic Plinian eruptions at the Las Sierras-Masaya caldera complex. Using the average bulk composition of the Fontana Lapilli eruption of Costantini et al., (2010), we investigated a wide parameter space, in which the oxygen fugacity (between NNO+1.3 and NNO−1.5), H_2O content (1 to 3 wt%), pressure (10 to 300 MPa) and temperature (1000 to 1150 °C) conditions were considered on the basis of the results obtained from previous studies (Costantini et al., 2010; Goepfert and Gardner, 2010; Szramek, 2016). The conditions that produced a comparable phenocryst crystal fraction with that observed in natural products were considered as possible pre-eruptive conditions. The Fontana Lapilli scoriae have ~5 vol% plagioclase, the dominant phenocryst phase, with ~1 vol% olivine and clinopyroxene. We find that the mineralogical assemblage and crystal content are produced at an oxygen fugacity of NNO -0.65, temperatures

~1050 °C, pressure between 45 and 65 MPa and H_2O content between 2 and 2.7 wt%. This range is comparable to the pre-eruptive condition determined by the hydrothermal phase equilibria experiments of Goepfert and Gardner (2010), which state that the Fontana Lapilli magma was last stored at 1010–1060 °C, 40–80 MPa with a H_2O content of 2–2.7 wt%. Due to the low H_2O concentrations of 1.4–1.9 wt% consistently measured in samples of the Fontana Lapilli eruption (Sadofsky et al., 2008; Wehrmann et al., 2011), the system is strongly water under-saturated at higher pressures of 100 to 300 MPa. Furthermore, clinopyroxene is the dominant crystallising phase at higher pressures, which is not compatible with the crystal assemblage observed in samples of the eruption (Costantini et al., 2010; Goepfert and Gardner, 2010; Szramek, 2016).

The pre-eruptive condition of the Fontana Lapilli eruption can therefore be considered comparable to the Masaya Triple Layer from the results of these simulations, with similar low stored H_2O concentrations of ~2 wt%, and temperatures <1100 °C. However, the pre-eruptive condition of the Masaya Triple Layer is at lower pressure and is more oxidised. Rhyolite-MELTS simulations investigating the control of oxygen fugacity on the observed crystal assemblage find that the oxygen fugacity of current activity at Masaya of NNO +0.98 (de Moor et al., 2013) is too oxidising to crystallise olivine from a magma with the Masaya Triple Layer bulk composition. Although it is difficult to determine the cause of the explosive-effusive transition of the Masaya system, it is evident that temperatures and oxygen fugacities of stored magma have changed through time. Pre-eruptive temperatures <1100 °C have been suggested as favourable for highly explosive basaltic activity due to the production of higher values of ΔT and syn-eruptive crystal content (Arzilli et al., 2019). The pre-eruptive temperature of the system may therefore have a crucial role in the evolution of the Masaya caldera complex and its explosive potential through time.

4.3.2. Syn-eruptive processes of explosive basaltic eruptions

Microlites resulting from large ΔT show significant disequilibrium textures and crystallised between 1 and 5 min during magma ascent, increasing magma viscosity from 10 Pa s to 10^6 Pa s. The rheological effects of microlite crystallisation have been previously documented for basaltic Plinian eruptions (e.g. Etna 122 BCE and 1886 Tarawera), where crystal fraction can reach 0.9 and 0.99 respectively (Houghton et al., 2004; Sable et al., 2006; Sable et al., 2009). At crystallinities exceeding 50 vol%, the viscosity of the magma is dominantly controlled by the crystal phase as opposed to the interstitial melt. Therefore, high crystal fractions observed in scoriae of basaltic Plinian eruptions suggest a significant change in rheological properties during ascent and enhanced explosivity (Houghton et al., 2004; Sable et al., 2006; Lavallée et al., 2007; Sable et al., 2009; Arzilli et al., 2019). In situ 4D crystallisation experiments combined with numerical simulations constrain a rapid timescale of syn-eruptive crystallisation for a basaltic Plinian eruption (Arzilli et al., 2019). Both CSD data and numerical modelling support rapid, syn-eruptive crystallisation and a concurrent rise in magma viscosity.

The distinctive textural heterogeneity of Masaya scoriae suggests regions of differing crystallinity may reflect different conditions during ascent. The high explosivity and dispersal of this Plinian eruption should preclude recycling of clasts (D'Oriano et al., 2014; Deardorff and Cashman, 2017), suggesting the textural heterogeneity is syn-eruptive in origin. Two possibilities include conduit zonation, as recorded in many explosive silicic eruptions, or alternatively the effects of mingling isochemical magmas having different thermal histories (Carrigan and Eichelberger, 1990; Polacci, 2005; Bouvet de Maissoneuve et al., 2009; Costantini et al., 2011). The irregular boundaries between crystalline domains could reflect an interface where there is mingling of cooler, more degassed and crystalline

magma with hotter, microlite-poor magma, potentially within the conduit due to a velocity gradient (Cimarelli et al., 2010). Lateral velocity gradients are a common feature of basaltic sub-Plinian to Plinian eruptions, and have been inferred for the Yufune-2, Fontana Lapilli and Etna 122 BCE eruptions where similar microtextural heterogeneity is observed (Sable et al., 2006; Suzuki and Fuji, 2010; Costantini et al., 2010). For the Masaya Triple Layer eruption, accumulation of crystalline, stagnating magma at the conduit walls could restrict the effective conduit radius, thereby enabling fragmentation whilst providing a channel for the fast ascent of crystal-poor magma. As this eruption is episodic, consisting of multiple stages of sub-Plinian to Plinian activity, temporal changes in the conduit radius may have contributed to the termination or renewal of explosivity, whilst restricting water access.

5. Conclusion and implications

We have constrained the pre and syn-eruptive conditions of the episodic Masaya Triple Layer basaltic Plinian eruption, which comprised several stages of Plinian and sub-Plinian magmatic and phreatomagmatic activity. Constraining these conditions is crucial to improve our understanding of basaltic Plinian volcanism, as these data underpin models of the triggering mechanism. Results from mineral-melt thermometers and Rhyolite-MELTS suggest that magma was last stored at 1080–1100 °C and 21–42 MPa prior to eruption, within a shallow reservoir at a depth of 0.8–1.6 km.

Within the conduit, the magma underwent significant changes in viscosity and rheology during ascent. The high microlite crystal fraction in scoriae, with hopper, skeletal and spherulitic morphologies, represents disequilibrium crystallisation resulting from large ΔT. Reaching 50 vol% crystallinity within 1–5 min of magma ascent induced a substantial rheological change, increasing the effective viscosity of the magma from 10 Pa s to 10^6 Pa s, approaching the fragmentation threshold. The brittle fragmentation model for high-viscosity silicic eruptions may therefore be analogous for basaltic systems under specific pre- and syn-eruptive conditions.

The basaltic Plinian activity at Masaya caldera shares many textural and depositional features with the Etna 122 BCE eruption, suggesting that basaltic Plinian eruptions may be promoted by a specific set of pre- and syn-eruptive physico-chemical magmatic conditions. Establishing how, why and when such conditions occur is an important consideration for hazard assessment at Masaya caldera. Furthermore, this suggests that other basaltic volcanoes that currently produce relatively benign low-explosivity eruptions could transform into highly explosive Plinian systems under the right conditions. The currently recognised examples of basaltic Plinian activity appear to share a range of parameters that contribute to their increased explosivity, with fast ascent rate, rapid crystallisation, moderate storage temperatures, low initial H_2O concentration, high microlite crystallinity, microtextural heterogeneity and velocity profiles having been identified or inferred for the Masaya Triple Layer, Fontana Lapilli, Etna 122 BCE and Tarawera eruptions (Houghton et al., 2004; Sable et al., 2006; Sable et al., 2009; Costantini et al., 2010; Goepfert and Gardner, 2010; Moitra et al., 2018; Arzilli et al., 2019). The unique combination of these parameters may have culminated in the explosive transformation of Masaya Volcano, whilst maintaining a compositionally homogeneous system through time. Whilst any or all of these parameters may increase the explosive potential, the difficulty in achieving all of these contributing factors simultaneously may explain the apparent rarity of basaltic Plinian eruptions in the geological record and the dominantly effusive activity of Masaya today.

Supplementary data to this article can be found online at https://doi.org/10.1016/j.jvolgeores.2019.106761.

CRediT authorship contribution statement

Emily C. Bamber: Conceptualization, Methodology, Investigation, Formal analysis, Writing - original draft, Writing - review & editing, Visualization, Supervision, Project administration. **Fabio Arzilli:** Conceptualization, Methodology, Investigation, Writing - original draft, Writing - review & editing, Visualization, Supervision. **Margherita Polacci:** Conceptualization, Investigation, Writing - original draft, Writing - review & editing, Visualization, Supervision. **Margaret E. Hartley:** Writing - original draft, Writing - review & editing, Visualization, Supervision. **Jonathan Fellowes:** Investigation. **Danilo Di Genova:** Investigation, Formal analysis, Writing - original draft, Writing - review & editing. **David Chavarría:** Resources. **José Armando Saballos:** Resources. **Mike R. Burton:** Conceptualization, Writing - original draft, Writing - review & editing, Visualization, Supervision, Funding acquisition, Project administration.

Declaration of competing interest

The authors declare that they have no known competing financial interests or personal relationships that could have appeared to influence the work reported in this paper.

Acknowledgements

References

Abramoff, M.D., Magalhães, P.J., Ram, S.J., 2004. Image processing with ImageJ. Biophoton. Int. 11 (7), 36–42.

Agostini, C., Fortunati, A., Arzilli, F., Landi, P., Carroll, M.R., 2013. Kinetics of crystal evolution as a probe to magmatism at Stromboli (Aeolian Archipelago, Italy). Geochim. Cosmochim. Acta 110, 135–151.

Aiuppa, A., Burton, M., Allard, P., Caltabiano, T., Giudice, G., Gurrieri, S., Liuzzo, M., Salerno, G., 2011. First observational evidence for the CO_2-driven origin of Stromboli's major explosions. Solid Earth 2, 135–142.

Alfano, F., Ort, M., Pioli, L., Self, S., Hanson, S., Roggensack, K., Allison, C., Amos, R., Clarke, A., 2018. Subplinian monogenetic basaltic eruption of Sunset Crater, Arizona, USA. GSA Bull. 131 (3–4), 661–674.

Allard, P., 2010. A CO_2-rich gas trigger of explosive paroxysms at Stromboli volcano, Italy. J. Volcanol. Geotherm. Res. 189, 363–374.

Allard, P., Burton, M., Muré, F., 2005. Spectroscopic evidence for a lava fountain driven by previously accumulated magmatic gas. Nature 433, 407–410.

Amante, C., Eakins, B.W., 2009. ETOPO1 1 Arc-Minute Global Relief Model: Procedures, Data sources and Analysis. NOAA Technical Memorandum NESDIS NGDC-24. National Geophysical Data Center, NOAA.

Armienti, P., Francalanci, L., Landi, P., 2007. Textural effects of steady state behaviour of the Stromboli feeding system. J. Volcanol. Geotherm. Res. 160 (1–2), 86–98.

Arzilli, F., Agostini, C., Landi, P., Fortunati, A., Mancini, L., Carroll, M., 2015. Plagioclase nucleation and growth kinetics in a hydrous basaltic melt by decompression experiments. Contrib. Mineral. Petrol. 170 (5–6).

Arzilli, F., Piochi, M., Mormone, A., Agostini, C., Carroll, M.R., 2016. Constraining pre-eruptive magma conditions and unrest timescales during the Monte Nuovo eruption (1538 AD; Campi Flegrei, Southern Italy): integrating textural and CSD results from experimental and natural trachy-phonolites. Bull. Volcanol. 78 (10), 72.

Arzilli, F., La Spina, G., Burton, M.R., Polacci, M., Le Gall, N., Hartley, M.E., Di Genova, D., Cai, B., Vo, N.T., Bamber, E.C., Nonni, S., Atwood, R., Llewellin, E.W., Brooker, R.A., Mader, H.M., Lee, P.D., 2019. Magma fragmentation in highly explosive basaltic eruptions induced by rapid crystallization. Nat. Geosci. 12, 1023–1028.

Arzilli, F., Morgavi, D., Petrelli, M., Polacci, M., Burton, M., Di Genova, D., Spina, L., La Spina, G., Hartley, M.E., Romero, J.E., Fellowes, J., Diaz-Alvarado, J., Perugini, D., 2019b. The unexpected explosive sub-Plinian eruption of Calbuco volcano (22–23 April 2015; southern Chile): triggering mechanism implications. J. Volcanol. Geotherm. Res. 378, 35–50.

Baker, D., Brun, F., O'Shaughnessy, C., Mancini, L., Fife, J., Rivers, M., 2012. A four-dimensional X-ray tomographic microscopy study of bubble growth in basaltic foam. Nat. Commun. 3 (1), 1135. https://doi.org/10.1038/ncomms2134.

Barth, A., Newcombe, M., Plank, T., Gonnermann, H., Hajimirza, S., Soto, G.J., Saballos, A., Hauri, E., 2019. Magma decompression rate correlates with explosivity at basaltic volcanoes – constraints from water diffusion in olivine. J. Volcanol. Geotherm. Res. 387, 106664.

Bice, D., 1985. Quaternary volcanic stratigraphy of Managua, Nicaragua: correlation and source assignment for multiple overlapping plinian deposits. Geol. Soc. Am. Bull. 96 (4), 553–566.

Blundy, J., Cashman, K.V., 2008. Petrologic reconstruction of magmatic system variables and processes In: Minerals, Inclusions and Volcanic Processes. Rev. Mineral. Geochem. 69, 179–239.

Blundy, J., Cashman, K.V., Rust, A., Witham, F., 2010. A case for CO_2-rich arc magmas. Earth Planet. Sci. Lett. 290, 289–301.

Bouvet de Maissoneuve, C., Bachmann, O., Burgisser, A., 2009. Characterization of juvenile pyroclasts from the Kos Plateau Tuff (Aegean Arc): insights into the eruptive dynamics of a large rhyolitic eruption. Bull. Volcanol. 71, 643–658.

Burton, M.R., Oppenheimer, C., Horrocks, L.A., Francis, P.W., 2000. Remote sensing of CO_2 and H_2O emission rates from Masaya volcano, Nicaragua. Geology 28 (10), 915–918.

Campagnola, S., Romano, C., Mastin, L.G., Vona, A., 2016. Confort 15 model of conduit dynamics: applications to Pantelleria Green Tuff and Etna 122 BC eruptions. Contrib. Mineral. Petrol. 171 (60).

Caplan-Auerbach, J., McNutt, S., 2003. New insights into the 1999 eruption of Shishaldin volcano, Alaska, based on acoustic data. Bull. Volcanol. 65 (6), 405–417.

Carrigan, C.R., Eichelberger, J.C., 1990. Zoning of magmas by viscosity in volcanic conduits. Nature 343, 248–251.

Cashman, K.V., 1988. Crystallization of Mount St. Helens 1980–1986 dacite: a quantitative textural approach. Bull. Volcanol. 50, 194–209.

Cashman, K.V., Marsh, B.D., 1988. Crystal size distribution (CSD) in rocks and the kinetics and dynamics of crystallization II: Makaopuhi lava lake. Contrib. Mineral. Petrol. 99, 292–305.

Cimarelli, C., Di Traglia, F., Taddeucci, J., 2010. Basaltic scoria textures from a zoned conduit as precursors to violent Strombolian activity. Geology 38 (5), 439–442.

Coltelli, M., Del Carlo, P., Vezzoli, L., 1998. Discovery of a Plinian basaltic eruption of Roman age at Etna volcano, Italy. Geology 26 (12), 1095–1098.

Costa, A., Caricchi, L., Bagdassarov, N., 2009. A model for the rheology of particle-bearing suspensions and partially molten rocks. Geochem. Geophys. Geosyst. 10 (3).

Costantini, L., Bonadonna, C., Houghton, B., Wehrmann, H., 2009. New physical characterization of the Fontana Lapilli basaltic Plinian eruption, Nicaragua. Bull. Volcanol. 71 (3), 337–355.

Costantini, L., Houghton, B., Bonadonna, C., 2010. Constraints on eruption dynamics of basaltic explosive activity derived from chemical and microtextural study: the example of the Fontana Lapilli Plinian eruption, Nicaragua. J. Volcanol. Geotherm. Res. 189 (3–4), 207–224.

Costantini, L., Pioli, L., Bonadonna, C., Clavero, J., Longchamp, C., 2011. A Late Holocene explosive mafic eruption of Villarrica volcano, Southern Andes: the Chaimilla deposit. J. Volcanol. Geotherm. Res. 200, 143–158.

Couch, S., 2003. Experimental investigation of crystallization kinetics in a haplogranite system. Am. Mineral. 88 (10), 1471–1485.

Cross, J.K., Tomlinson, E.L., Giordano, G., Smith, V.C., De Benedetti, A.A., Roberge, J., Manning, C.J., Wulf, S., Menzies, M.A., 2014. High level triggers for explosive mafic volcanism: Albano Maar, Italy. Lithos 190-191, 137–153.

Dallai, L., Cioni, R., Boschi, C., D'Oriano, C., 2011. Carbonate-derived CO_2 purging magma at depth: Influence on the eruptive activity of Somma-Vesuvius, Italy. Earth Planet. Sci. Lett. 310 (1–2), 84–95.

de Moor, J.M., Fischer, T.P., Sharp, Z.D., King, P.L., Wilke, M., Botcharnikov, R.E., Cottrell, E., Zelenski, M., Marty, B., Klimm, K., Rivard, C., 2013. Sulphur degassing at Erta Ale (Ethiopia) and Masaya (Nicaragua) volcanoes: Implications for degassing processes and oxygen fugacities of basaltic systems. Geochem. Geophys. Geosyst. 14, 4076–4108.

Deardorff, N., Cashman, K., 2017. Rapid crystallization during recycling of basaltic andesite tephra: timescales determined by reheating experiments. Sci. Rep. 7 (1), 46364. https://doi.org/10.1038/srep46364.

Del Carlo, P., Pompilio, M., 2004. The relationship between volatile content and the eruptive style of basaltic magma: the Etna case. Ann. Geophys. 47 (4). https://doi.org/10.4401/ag-4402.

Di Genova, D., Sicola, S., Romano, C., Vona, A., Fanara, S., Spina, L., 2017. Effect of iron and nanolites on Raman spectra of volcanic glasses: a reassessment of existing strategies to estimate the water content. Chem. Geol. 475, 76–86.

Dingwell, D., 1996. Volcanic Dilemma–Flow or Blow? Science 273 (5278), 1054–1055.

D'Oriano, C., Bertagnini, A., Cioni, R., Pompilio, M., 2014. Identifying recycled ash in basaltic eruptions. Sci. Rep. 4 (1), 5851. https://doi.org/10.1038/srep05851.

Duffell, H.J., Oppenheimer, C., Pyle, D.M., Galle, B., McGonigle, A.J.S., Burton, M.R., 2003. Changes in gas composition prior to a minor explosive eruption at Masaya volcano, Nicaragua. J. Volcanol. Geotherm. Res. 126 (3–4), 327–339.

Fornaciai, A., Landi, P., Armienti, P., 2009. Dissolution/crystallization kinetics recorded in the 2002–2003 lavas of Stromboli (Italy). Bull. Volcanol. 71 (6), 631–641.

Freda, C., Gaeta, M., Giaccio, B., Marra, F., Palladino, D.M., Scarlato, P., Sottili, G., 2011. CO_2-driven large mafic explosive eruptions: the Pozzolane Rosse case study from the Colli Albani Volcanic District (Italy). Bull. Volcanol. 73, 241–256.

Freundt, A., Kutterolf, S., Schmincke, H.-U., Hansteen, T., Wehrmann, W., Pérez, W., Strauch, W., Navarro, M., 2006. Volcanic hazards in Nicaragua: past, present and future. Volcanic Hazards in Central America. Special Paper 412. The Geological Society of America, Boulder, pp. 141–166.

Giordano, D., Dingwell, D., 2003. Viscosity of hydrous Etna basalt: implications for Plinian-style basaltic eruptions. Bull. Volcanol. 65 (1), 8–14.

Giordano, D., Russell, J., Dingwell, D., 2008. Viscosity of magmatic liquids: a model. Earth Planet. Sci. Lett. 271 (1–4), 123–134.

Goepfert, K., Gardner, J., 2010. Influence of pre-eruptive storage conditions and volatile contents on explosive Plinian style eruptions of basic magma. Bull. Volcanol. 72 (5), 511–521.

Grove, T.L., Baker, M.B., 1984. Phase equilibrium controls on the tholeiitic versus calc-alkaline differentiation trends. J. Geophys. Res. 89 (B5), 3253–3274.

Gualda, G., Ghiorso, M., Lemons, R., Carley, T., 2012. Rhyolite-MELTS: a Modified Calibration of MELTS Optimized for Silica-rich, Fluid-bearing Magmatic Systems. J. Petrol. 53 (5), 875–890.

Hammer, J.E., Cashman, K.V., Hoblitt, R.P., Newman, S., 1999. Degassing and microlite crystallization during pre-climactic events of the 1991 eruption of Mt. Pinatubo, Philippines. Bull. Volcanol. 60, 355–380.

Hammer, J., Rutherford, M., 2002. An experimental study of the kinetics of decompression-induced crystallization in silicic melt. Journal of Geophysical Research: Solid Earth 107 (B1).

Higgins, M.D., 2000. Measurements of crystal size distributions. Am. Mineral. 85, 1105–1116.

Higgins, M.D., 2002. Closure in crystal size distributions (CSD), verification of CSD calculations, and the significance of CSD fans. Am. Mineral. 87, 171–175.

Houghton, B.F., Gonnermann, H.M., 2008. Basaltic explosive volcanism: constraints from deposits and models. Chem. Erde 68, 117–140.

Houghton, B.F., Wilson, C., Del Carlo, P., Coltelli, M., Sable, J., Carey, R., 2004. The influence of conduit processes on changes in style of basaltic Plinian eruptions: Tarawera 1886 and Etna 122 BC. J. Volcanol. Geotherm. Res. 137 (1–3), 1–14.

Kennedy, B.M., Jellinek, A.M., Russell, J.K., Nichols, A.R.L., Vigouroux, N., 2010. Time-and temperature-dependent conduit wall porosity: a key control on degassing and explosivity at Tarawera volcano, New Zealand. Earth Planet. Sci. Lett. 299, 126–137.

Kutterolf, S., Freundt, A., Pérez, W., Wehrmann, H., Schmincke, H., 2007. Late Pleistocene to Holocene temporal succession and magnitudes of highly-explosive volcanic eruptions in west-central Nicaragua. J. Volcanol. Geotherm. Res. 163 (1–4), 55–82.

Kutterolf, S., Freundt, A., Peréz, W., Mörz, T., Schacht, U., Wehrmann, H., Schmincke, H., 2008. Pacific offshore record of plinian arc volcanism in Central America: 1. Along-arc correlations. Geochem. Geophys. Geosyst. 9 (2).

La Felice, S., Landi, P., 2011. The 2009 paroxysmal explosions at Stromboli (Italy): magma mixing and eruption dynamics. Bull. Volcanol. 73, 1147–1154.

La Spina, G., Burton, M., de'Michieli Vitturi, M., Arzilli, F., 2016. Role of syn-eruptive plagioclase disequilibrium crystallization in basaltic magma ascent dynamics. Nat. Commun. 7, 13402. https://doi.org/10.1038/ncomms13402.

Lavallée, Y., Hess, K.-U., Cordonnier, B., Dingwell, D.B., 2007. Non-Newtonian rheological law for highly crystalline dome lavas. Geology 35 (9), 843–846.

Lloyd, A., Plank, T., Ruprecht, P., Hauri, E., Rose, W., 2013. Volatile loss from melt inclusions in pyroclasts of differing sizes. Contrib. Mineral. Petrol. 165 (1), 129–153.

Lofgren, G., 1974. An experimental study of plagioclase crystal morphology; isothermal crystallization. Am. J. Sci. 274 (3), 243–273.

Lofgren, G., 1980. Experimental studies on the dynamic crystallisation of silicate melts. In: Hargreaves, R.B. (Ed.), Physics of Magmatic Processes. Princeton University Press, Princeton, pp. 487–551.

Long, D.A., 1977. Raman Spectroscopy. vol. 2. McGraw-Hill, p. 276.

Mangler, M.F., Prytulak, J., Gisbert, G., Delgado-Granados, H., Petrone, C.M., 2019. Interplinian effusive activity at Popocatépetl volcano, Mexico: new insights into evolution and dynamics of the plumbing system. Volcanica 2 (1), 45–72.

Marsh, B.D., 1988. Crystal size distribution (CSD) in rocks and the kinetics and dynamics of crystallization: I. Theory. Contrib. Mineral. Petrol. 99, 277–291.

Marsh, B.D., 1998. On the interpretation of crystal size distributions in magmatic systems. J. Petrol. 39, 553–599.

Métaxian, J.-P., 1994. Étude Sismologique et Gravimétriqe d'un Volcan Actif: Dynamisme Interne et Structure de la Caldera Masaya, Nicaragua. Université de Savoie (319 pp).

Métaxian, J.-P., Lesage, P., Dorel, J., 1997. Permanent tremor of Masaya Volcano, Nicaragua: wave field analysis and source location. J. Geophys. Res. 102, 22529–22545.

Moitra, P., Gonnermann, H., Houghton, B., Tiwary, C., 2018. Fragmentation and Plinian eruption of crystallizing basaltic magma. Earth Planet. Sci. Lett. 500, 97–104.

Moore, G., Vennemann, T., Carmichael, I.S.E., 1998. An empirical model for solubility of H_2O in magmas to 3 kilobars. Am. Mineral. 83, 36–42.

Morgan, D., Jerram, D., 2006. On estimating crystal shape for crystal size distribution analysis. J. Volcanol. Geotherm. Res. 154 (1–2), 1–7.

Namiki, A., Manga, M., 2008. Transition between fragmentation and permeable outgassing of low viscosity magmas. J. Volcanol. Geotherm. Res. 169 (1–2), 48–60.

Newhall, C., Self, S., 1982. The volcanic explosivity index (VEI) an estimate of explosive magnitude for historical volcanism. J. Geophys. Res. 87 (C2).

Obermann, A., Molinari, I., Métaxian, J.-P., Grigoli, F., Strauch, W., Wiemer, S., 2019. Structure of Masaya and Momotombo volcano, Nicaragua, investigated with a temporary seismic network. J. Volcanol. Geotherm. Res. 379, 1–11.

Papale, P., 1999. Strain-induced magma fragmentation in explosive eruptions. Nature 397 (6718), 425–428.

Parfitt, E., 2004. A discussion of the mechanisms of explosive basaltic eruptions. J. Volcanol. Geotherm. Res. 134 (1–2), 77–107.

Pérez, W., Freundt, A., 2006. The youngest highly explosive basaltic eruptions from Masaya Caldera (Nicaragua): Stratigraphy and hazard assessment. Volcanic Hazards in Central America. Special Paper 412. The Geological Society of America, Boulder, pp. 189–208.

Pérez, W., Freundt, A., Kutterolf, S., Schmincke, H., 2009. The Masaya Triple Layer: a 2100 year old basaltic multi-episodic Plinian eruption from the Masaya Caldera Complex (Nicaragua). J. Volcanol. Geotherm. Res. 179 (3–4), 191–205.

Polacci, M., 2005. Constraining the dynamics of volcanic eruptions by characterization of pumice textures. Ann. Geophys. 48, 731–738.

Polacci, M., Arzilli, F., La Spina, G., Le Gall, N., Cai, B., Hartley, M.E., Di Genova, D., Vo, N.T., Nonni, S., Atwood, R.C., Llewellin, E.W., Lee, P.D., Burton, M.R., 2018. Crystallisation in basaltic magmas revealed via in situ 4D synchrotron X-ray microtomography. Sci. Rep. 8 (1), 8377. https://doi.org/10.1038/s41598-018-26644-6.

Potts, P.J., Webb, P.C., 1992. X-ray fluorescence spectrometry. J. Geochem. Explor. 44, 251–296.

Putirka, K., 2008. Thermometers and barometers for volcanic systems. Rev. Mineral. Geochem. 69 (1), 61–120.

Sable, J., Houghton, B., Del Carlo, P., Coltelli, M., 2006. Changing conditions of magma ascent and fragmentation during the Etna 122 BC basaltic Plinian eruption: evidence from clast microtextures. J. Volcanol. Geotherm. Res. 158 (3–4), 333–354.

Sable, J., Houghton, B., Wilson, C., Carey, R., 2009. Eruption mechanisms during the climax of the Tarawera 1886 basaltic Plinian eruption inferred from microtextural characteristics of the deposits. In: Thordarson, T., Self, S., Larsen, G., Rowland, S., Hoskuldsson, A. (Eds.), Studies in Volcanology: The Legacy of George Walker. Special Publications of IAVCEI. The Geological Society of London, London, pp. 129–153.

Sadofsky, S., Portnyagin, M., Hoernle, K., van den Bogaard, P., 2008. Subduction cycling of volatiles and trace elements through the Central American volcanic arc: evidence from melt inclusions. Contrib. Mineral. Petrol. 155 (4), 433–456.

Schauroth, J., Wadsworth, F., Kennedy, B., von Aulock, F., Lavallée, Y., Damby, D., Vasseur, J., Scheu, B., Dingwell, D., 2016. Conduit margin heating and deformation during the AD 1886 basaltic Plinian eruption at Tarawera volcano, New Zealand. Bull. Volcanol. 78 (2).

Schmincke, H., Kutterolf, S., Pérez, W., Rausch, J., Freundt, A., Strauch, W., 2009. Walking through volcanic mud: the 2100-year-old Acahualinca footprints (Nicaragua) I: Stratigraphy, lithology, and volcanology and age of the Acahualinca section. Bull. Volcanol. 71 (5), 479–493.

Schmincke, H., Rausch, J., Kutterolf, S., Freundt, A., 2010. Walking through volcanic mud: the 2100 year-old Acahualinca footprints (Nicaragua) II: the Acahualinca people, environmental conditions and motivation. Int. J. Earth Sci. 99, S279–S292.

Schneider, C.A., Rasband, W.S., Eliceiri, K.W., 2012. NIH image to ImageJ: 25 years of image analysis. Nat. Methods 9, 671–675.

Shea, T., Hammer, J., 2013. Kinetics of cooling- and decompression-induced crystallization in hydrous mafic-intermediate magmas. J. Volcanol. Geotherm. Res. 260, 127–145.

Stelling, P., Beget, J., Nye, C., Gardner, J., Devine, J.D., George, R.M.M., 2002. Geology and petrology of ejecta from the 1999 eruption of Shishaldin Volcano, Alaska. Bull. Volcanol. 64 (8), 548–561.

Stoiber, R.E., Williams, S.N., Huebert, B.J., 1986. Sulfur and halogen gases at Masaya Caldera complex, Nicaragua: Total flux and variations with time. J. Geophys. Res. 91 (B12), 12215–12231.

Suzuki, Y., Fujii, T., 2010. Effect of syneruptive decompression path on shifting intensity in basaltic sub-Plinian eruption: Implication of microlites in Yufune-2 scoria from Fuji volcano, Japan. J. Volcanol. Geotherm. Res. 198 (1–2), 158–176.

Swanson, D.A., Rose, T.R., Fiske, R.S., McGeehin, J.P., 2012. Keanakāko'i Tephra produced by 300 years of explosive eruptions following collapse of Kīlauea's caldera in about 1500 CE. J. Volcanol. Geotherm. Res. 215–216, 8–25.

Szramek, L., 2016. Mafic Plinian eruptions: is fast ascent required? Journal of Geophysical Research: Solid Earth 121 (10), 7119–7136.

Szramek, L., Gardner, J., Larsen, J., 2006. Degassing and microlite crystallization of basaltic andesite magma erupting at Arenal Volcano, Costa Rica. J. Volcanol. Geotherm. Res. 157 (1–3), 182–201.

Szramek, L., Gardner, J., Hort, M., 2010. Cooling-induced crystallization of microlite crystals in two basaltic pumice clasts. Am. Mineral. 95 (4), 503–509.

Vona, A., Romano, C., Dingwell, D., Giordano, D., 2011. The rheology of crystal-bearing basaltic magmas from Stromboli and Etna. Geochim. Cosmochim. Acta 75 (11), 3214–3323.

Walker, J.A., 1989. Caribbean arc theoliites. J. Geophys. Res. 94 (B4), 10539–10548.

Walker, J.A., Williams, S.N., Kalamarides, R.I., Feigenson, M.D., 1993. Shallow open-system evolution of basaltic magma beneath a subduction zone volcano: the Masaya Caldera Complex, Nicaragua. J. Volcanol. Geotherm. Res. 56, 379–400.

Wehrmann, H., Bonadonna, C., Freundt, A., Houghton, B.F., Kutterolf, S., 2006. Fontana Tephra: A basaltic Plinian eruption in Nicaragua. Volcanic Hazards in Central America. Special Paper 412. The Geological Society of America, Boulder, pp. 189–208.

Wehrmann, H., Hoernle, K., Portnyagin, M., Wiedenbeck, M., Heydolph, K., 2011. Volcanic CO_2 output at the Central American subduction zone inferred from melt inclusions in olivine crystals from mafic tephras. Geochemistry Geophysics Geosystems 12, Q06003.

Williams, S.N., 1983. Plinian airfall deposits of basaltic composition. Geology 11, 211–214.

Williams-Jones, G., Rymer, H., Rothery, D.A., 2003. Gravity changes and passive SO_2 degassing at the Masaya caldera complex, Nicaragua. J. Volcanol. Geotherm. Res. 123, 137–160.

Wilson, S.A., 2000. Data Compilation for USGS Reference Material BHVO-2. U.S.G.S, Hawaiian Basalt (Open file report).

Wilson, L., Head, J.W., 1994. Mars: Review and analysis of volcanic eruption theory and relationships to observed landforms. Rev. Geophys. 32 (3), 221–263.

Zhang, Y., 1999. A criterion for the fragmentation of bubbly magma based on brittle failure theory. Nature 402, 648–650.

Zurek, J., Moune, S., Williams-Jones, G., Vigouroux, N., Gauthier, P.-J., 2019. Melt inclusion evidence for long term steady-state volcanism at Las Sierras-Masaya volcano, Nicaragua. J. Volcanol. Geotherm. Res. 378, 16–28.